Identified charged hadron production in $p+p$ collisions at $\sqrt{s}$ = 200 and 62.4 GeV

A. Adare,[11] S. Afanasiev,[25] C. Aidala,[12, 36] N.N. Ajitanand,[53] Y. Akiba,[47, 48] H. Al-Bataineh,[42] J. Alexander,[53] K. Aoki,[30, 47] L. Aphecetche,[55] R. Armendariz,[42] S.H. Aronson,[6] J. Asai,[47, 48] E.T. Atomssa,[31] R. Averbeck,[54] T.C. Awes,[43] B. Azmoun,[6] V. Babintsev,[21] M. Bai,[5] G. Baksay,[17] L. Baksay,[17] A. Baldisseri,[14] K.N. Barish,[7] P.D. Barnes,[33] B. Bassalleck,[41] A.T. Basye,[1] S. Bathe,[7] S. Batsouli,[43] V. Baublis,[46] C. Baumann,[37] A. Bazilevsky,[6] S. Belikov,[6, *] R. Bennett,[54] A. Berdnikov,[50] Y. Berdnikov,[50] A.A. Bickley,[11] J.G. Boissevain,[33] H. Borel,[14] K. Boyle,[54] M.L. Brooks,[33] H. Buesching,[6] V. Bumazhnov,[21] G. Bunce,[6, 48] S. Butsyk,[33, 54] C.M. Camacho,[33] S. Campbell,[54] B.S. Chang,[62] W.C. Chang,[2] J.-L. Charvet,[14] S. Chernichenko,[21] J. Chiba,[26] C.Y. Chi,[12] M. Chiu,[22] I.J. Choi,[62] R.K. Choudhury,[4] T. Chujo,[58, 59] P. Chung,[53] A. Churyn,[21] V. Cianciolo,[43] Z. Citron,[54] C.R. Cleven,[19] B.A. Cole,[12] M.P. Comets,[44] P. Constantin,[33] M. Csanád,[16] T. Csörgő,[27] T. Dahms,[54] S. Dairaku,[30, 47] K. Das,[18] G. David,[6] M.B. Deaton,[1] K. Dehmelt,[17] H. Delagrange,[55] A. Denisov,[21] D. d'Enterria,[12, 31] A. Deshpande,[48, 54] E.J. Desmond,[6] O. Dietzsch,[51] A. Dion,[54] M. Donadelli,[51] O. Drapier,[31] A. Drees,[54] K.A. Drees,[5] A.K. Dubey,[61] A. Durum,[21] D. Dutta,[4] V. Dzhordzhadze,[7] Y.V. Efremenko,[43] J. Egdemir,[54] F. Ellinghaus,[11] W.S. Emam,[7] T. Engelmore,[12] A. Enokizono,[32] H. En'yo,[47, 48] S. Esumi,[58] K.O. Eyser,[7] B. Fadem,[38] D.E. Fields,[41, 48] M. Finger, Jr.,[8, 25] M. Finger,[8, 25] F. Fleuret,[31] S.L. Fokin,[29] Z. Fraenkel,[61, *] J.E. Frantz,[54] A. Franz,[6] A.D. Frawley,[18] K. Fujiwara,[47] Y. Fukao,[30, 47] T. Fusayasu,[40] S. Gadrat,[34] I. Garishvili,[56] A. Glenn,[11] H. Gong,[54] M. Gonin,[31] J. Gosset,[14] Y. Goto,[47, 48] R. Granier de Cassagnac,[31] N. Grau,[12, 24] S.V. Greene,[59] M. Grosse Perdekamp,[22, 48] T. Gunji,[10] H.-Å. Gustafsson,[35, *] T. Hachiya,[20] A. Hadj Henni,[55] C. Haegemann,[41] J.S. Haggerty,[6] H. Hamagaki,[10] R. Han,[45] H. Harada,[20] E.P. Hartouni,[32] K. Haruna,[20] E. Haslum,[35] R. Hayano,[10] M. Heffner,[32] T.K. Hemmick,[54] T. Hester,[7] X. He,[19] H. Hiejima,[22] J.C. Hill,[24] R. Hobbs,[41] M. Hohlmann,[17] W. Holzmann,[53] K. Homma,[20] B. Hong,[28] T. Horaguchi,[10, 47, 57] D. Hornback,[56] S. Huang,[59] T. Ichihara,[47, 48] R. Ichimiya,[47] H. Iinuma,[30, 47] Y. Ikeda,[58] K. Imai,[30, 47] J. Imrek,[15] M. Inaba,[58] Y. Inoue,[49, 47] D. Isenhower,[1] L. Isenhower,[1] M. Ishihara,[47] T. Isobe,[10] M. Issah,[53] A. Isupov,[25] D. Ivanischev,[46] B.V. Jacak,[54, †] J. Jia,[12] J. Jin,[12] O. Jinnouchi,[48] B.M. Johnson,[6] K.S. Joo,[39] D. Jouan,[44] F. Kajihara,[10] S. Kametani,[10, 47, 60] N. Kamihara,[47, 48] J. Kamin,[54] M. Kaneta,[48] J.H. Kang,[62] H. Kanou,[47, 57] J. Kapustinsky,[33] D. Kawall,[36, 48] A.V. Kazantsev,[29] T. Kempel,[24] A. Khanzadeev,[46] K.M. Kijima,[20] J. Kikuchi,[60] B.I. Kim,[28] D.H. Kim,[39] D.J. Kim,[62] E. Kim,[52] S.H. Kim,[62] E. Kinney,[11] K. Kiriluk,[11] Á. Kiss,[16] E. Kistenev,[6] A. Kiyomichi,[47] J. Klay,[32] C. Klein-Boesing,[37] L. Kochenda,[46] V. Kochetkov,[21] B. Komkov,[46] M. Konno,[58] J. Koster,[22] D. Kotchetkov,[7] A. Kozlov,[61] A. Král,[13] A. Kravitz,[12] J. Kubart,[8, 23] G.J. Kunde,[33] N. Kurihara,[10] K. Kurita,[49, 47] M. Kurosawa,[47] M.J. Kweon,[28] Y. Kwon,[56, 62] G.S. Kyle,[42] R. Lacey,[53] Y.S. Lai,[12] J.G. Lajoie,[24] D. Layton,[22] A. Lebedev,[24] D.M. Lee,[33] K.B. Lee,[28] M.K. Lee,[62] T. Lee,[52] M.J. Leitch,[33] M.A.L. Leite,[51] B. Lenzi,[51] P. Liebing,[48] T. Liška,[13] A. Litvinenko,[25] H. Liu,[42] M.X. Liu,[33] X. Li,[9] B. Love,[59] D. Lynch,[6] C.F. Maguire,[59] Y.I. Makdisi,[5] A. Malakhov,[25] M.D. Malik,[41] V.I. Manko,[29] E. Mannel,[12] Y. Mao,[45, 47] L. Mašek,[8, 23] H. Masui,[58] F. Matathias,[12] M. McCumber,[54] P.L. McGaughey,[33] N. Means,[54] B. Meredith,[22] Y. Miake,[58] P. Mikeš,[8, 23] K. Miki,[58] T.E. Miller,[59] A. Milov,[6, 54] S. Mioduszewski,[6] M. Mishra,[3] J.T. Mitchell,[6] M. Mitrovski,[53] A.K. Mohanty,[4] Y. Morino,[10] A. Morreale,[7] D.P. Morrison,[6] T.V. Moukhanova,[29] D. Mukhopadhyay,[59] J. Murata,[49, 47] S. Nagamiya,[26] Y. Nagata,[58] J.L. Nagle,[11] M. Naglis,[61] M.I. Nagy,[16] I. Nakagawa,[47, 48] Y. Nakamiya,[20] T. Nakamura,[20] K. Nakano,[47, 57] J. Newby,[32] M. Nguyen,[54] T. Niita,[58] B.E. Norman,[33] R. Nouicer,[6] A.S. Nyanin,[29] E. O'Brien,[6] S.X. Oda,[10] C.A. Ogilvie,[24] H. Ohnishi,[47] K. Okada,[48] M. Oka,[58] O.O. Omiwade,[1] Y. Onuki,[47] M. Ouchida,[20] K. Ozawa,[10] R. Pak,[6] D. Pal,[59] A.P.T. Palounek,[33] V. Pantuev,[54] V. Papavassiliou,[42] J. Park,[52] W.J. Park,[28] S.F. Pate,[42] H. Pei,[24] J.-C. Peng,[22] H. Pereira,[14] V. Peresedov,[25] D.Yu. Peressounko,[29] C. Pinkenburg,[6] M.L. Purschke,[6] A.K. Purwar,[33] H. Qu,[19] J. Rak,[41] A. Rakotozafindrabe,[31] I. Ravinovich,[61] K.F. Read,[43, 56] S. Rembeczki,[17] M. Reuter,[54] K. Reygers,[37] V. Riabov,[46] Y. Riabov,[46] D. Roach,[59] G. Roche,[34] S.D. Rolnick,[7] A. Romana,[31, *] M. Rosati,[24] S.S.E. Rosendahl,[35] P. Rosnet,[34] P. Rukoyatkin,[25] P. Ružička,[23] V.L. Rykov,[47] B. Sahlmueller,[37] N. Saito,[30, 47, 48] T. Sakaguchi,[6] S. Sakai,[58] K. Sakashita,[47, 57] H. Sakata,[20] V. Samsonov,[46] S. Sato,[26] T. Sato,[58] S. Sawada,[26] K. Sedgwick,[7] J. Seele,[11] R. Seidl,[22] A.Yu. Semenov,[24] V. Semenov,[21] R. Seto,[7] D. Sharma,[61] I. Shein,[21] A. Shevel,[46, 53] T.-A. Shibata,[47, 57] K. Shigaki,[20] M. Shimomura,[58] K. Shoji,[30, 47] P. Shukla,[4] A. Sickles,[6, 54] C.L. Silva,[51] D. Silvermyr,[43] C. Silvestre,[14] K.S. Sim,[28] B.K. Singh,[3] C.P. Singh,[3] V. Singh,[3] S. Skutnik,[24] M. Slunečka,[8, 25] A. Soldatov,[21] R.A. Soltz,[32] W.E. Sondheim,[33] S.P. Sorensen,[56] I.V. Sourikova,[6] F. Staley,[14] P.W. Stankus,[43] E. Stenlund,[35] M. Stepanov,[42] A. Ster,[27] S.P. Stoll,[6] T. Sugitate,[20] C. Suire,[44] A. Sukhanov,[6] J. Sziklai,[27] T. Tabaru,[48] S. Takagi,[58] E.M. Takagui,[51] A. Taketani,[47, 48] R. Tanabe,[58] Y. Tanaka,[40] K. Tanida,[47, 48, 52] M.J. Tannenbaum,[6] A. Taranenko,[53] P. Tarján,[15] H. Themann,[54] T.L. Thomas,[41] M. Togawa,[30, 47] A. Toia,[54] J. Tojo,[47] L. Tomášek,[23] Y. Tomita,[58] H. Torii,[20, 47] R.S. Towell,[1] V-N. Tram,[31]

I. Tserruya,[61] Y. Tsuchimoto,[20] C. Vale,[24] H. Valle,[59] H.W. van Hecke,[33] A. Veicht,[22] J. Velkovska,[59] R. Vértesi,[15] A.A. Vinogradov,[29] M. Virius,[13] V. Vrba,[23] E. Vznuzdaev,[46] M. Wagner,[30, 47] D. Walker,[54] X.R. Wang,[42] Y. Watanabe,[47, 48] F. Wei,[24] J. Wessels,[37] S.N. White,[6] D. Winter,[12] C.L. Woody,[6] M. Wysocki,[11] W. Xie,[48] Y.L. Yamaguchi,[60] K. Yamaura,[20] R. Yang,[22] A. Yanovich,[21] Z. Yasin,[7] J. Ying,[19] S. Yokkaichi,[47, 48] G.R. Young,[43] I. Younus,[41] I.E. Yushmanov,[29] W.A. Zajc,[12] O. Zaudtke,[37] C. Zhang,[43] S. Zhou,[9] J. Zimányi,[27, *] and L. Zolin[25]

(PHENIX Collaboration)

[1]*Abilene Christian University, Abilene, Texas 79699, USA*
[2]*Institute of Physics, Academia Sinica, Taipei 11529, Taiwan*
[3]*Department of Physics, Banaras Hindu University, Varanasi 221005, India*
[4]*Bhabha Atomic Research Centre, Bombay 400 085, India*
[5]*Collider-Accelerator Department, Brookhaven National Laboratory, Upton, New York 11973-5000, USA*
[6]*Physics Department, Brookhaven National Laboratory, Upton, New York 11973-5000, USA*
[7]*University of California - Riverside, Riverside, California 92521, USA*
[8]*Charles University, Ovocný trh 5, Praha 1, 116 36, Prague, Czech Republic*
[9]*China Institute of Atomic Energy (CIAE), Beijing, People's Republic of China*
[10]*Center for Nuclear Study, Graduate School of Science, University of Tokyo, 7-3-1 Hongo, Bunkyo, Tokyo 113-0033, Japan*
[11]*University of Colorado, Boulder, Colorado 80309, USA*
[12]*Columbia University, New York, New York 10027 and Nevis Laboratories, Irvington, New York 10533, USA*
[13]*Czech Technical University, Zikova 4, 166 36 Prague 6, Czech Republic*
[14]*Dapnia, CEA Saclay, F-91191, Gif-sur-Yvette, France*
[15]*Debrecen University, H-4010 Debrecen, Egyetem tér 1, Hungary*
[16]*ELTE, Eötvös Loránd University, H - 1117 Budapest, Pázmány P. s. 1/A, Hungary*
[17]*Florida Institute of Technology, Melbourne, Florida 32901, USA*
[18]*Florida State University, Tallahassee, Florida 32306, USA*
[19]*Georgia State University, Atlanta, Georgia 30303, USA*
[20]*Hiroshima University, Kagamiyama, Higashi-Hiroshima 739-8526, Japan*
[21]*IHEP Protvino, State Research Center of Russian Federation, Institute for High Energy Physics, Protvino, 142281, Russia*
[22]*University of Illinois at Urbana-Champaign, Urbana, Illinois 61801, USA*
[23]*Institute of Physics, Academy of Sciences of the Czech Republic, Na Slovance 2, 182 21 Prague 8, Czech Republic*
[24]*Iowa State University, Ames, Iowa 50011, USA*
[25]*Joint Institute for Nuclear Research, 141980 Dubna, Moscow Region, Russia*
[26]*KEK, High Energy Accelerator Research Organization, Tsukuba, Ibaraki 305-0801, Japan*
[27]*KFKI Research Institute for Particle and Nuclear Physics of the Hungarian Academy of Sciences (MTA KFKI RMKI), H-1525 Budapest 114, POBox 49, Budapest, Hungary*
[28]*Korea University, Seoul, 136-701, Korea*
[29]*Russian Research Center "Kurchatov Institute", Moscow, 123098 Russia*
[30]*Kyoto University, Kyoto 606-8502, Japan*
[31]*Laboratoire Leprince-Ringuet, Ecole Polytechnique, CNRS-IN2P3, Route de Saclay, F-91128, Palaiseau, France*
[32]*Lawrence Livermore National Laboratory, Livermore, California 94550, USA*
[33]*Los Alamos National Laboratory, Los Alamos, New Mexico 87545, USA*
[34]*LPC, Université Blaise Pascal, CNRS-IN2P3, Clermont-Fd, 63177 Aubiere Cedex, France*
[35]*Department of Physics, Lund University, Box 118, SE-221 00 Lund, Sweden*
[36]*Department of Physics, University of Massachusetts, Amherst, Massachusetts 01003-9337, USA*
[37]*Institut für Kernphysik, University of Muenster, D-48149 Muenster, Germany*
[38]*Muhlenberg College, Allentown, Pennsylvania 18104-5586, USA*
[39]*Myongji University, Yongin, Kyonggido 449-728, Korea*
[40]*Nagasaki Institute of Applied Science, Nagasaki-shi, Nagasaki 851-0193, Japan*
[41]*University of New Mexico, Albuquerque, New Mexico 87131, USA*
[42]*New Mexico State University, Las Cruces, New Mexico 88003, USA*
[43]*Oak Ridge National Laboratory, Oak Ridge, Tennessee 37831, USA*
[44]*IPN-Orsay, Universite Paris Sud, CNRS-IN2P3, BP1, F-91406, Orsay, France*
[45]*Peking University, Beijing, People's Republic of China*
[46]*PNPI, Petersburg Nuclear Physics Institute, Gatchina, Leningrad region, 188300, Russia*
[47]*RIKEN Nishina Center for Accelerator-Based Science, Wako, Saitama 351-0198, Japan*
[48]*RIKEN BNL Research Center, Brookhaven National Laboratory, Upton, New York 11973-5000, USA*
[49]*Physics Department, Rikkyo University, 3-34-1 Nishi-Ikebukuro, Toshima, Tokyo 171-8501, Japan*
[50]*Saint Petersburg State Polytechnic University, St. Petersburg, 195251 Russia*
[51]*Universidade de São Paulo, Instituto de Física, Caixa Postal 66318, São Paulo CEP05315-970, Brazil*
[52]*Seoul National University, Seoul, Korea*
[53]*Chemistry Department, Stony Brook University, SUNY, Stony Brook, New York 11794-3400, USA*
[54]*Department of Physics and Astronomy, Stony Brook University, SUNY, Stony Brook, New York 11794-3400, USA*
[55]*SUBATECH (Ecole des Mines de Nantes, CNRS-IN2P3, Université de Nantes) BP 20722 - 44307, Nantes, France*

^{56}*University of Tennessee, Knoxville, Tennessee 37996, USA*
^{57}*Department of Physics, Tokyo Institute of Technology, Oh-okayama, Meguro, Tokyo 152-8551, Japan*
^{58}*Institute of Physics, University of Tsukuba, Tsukuba, Ibaraki 305, Japan*
^{59}*Vanderbilt University, Nashville, Tennessee 37235, USA*
^{60}*Waseda University, Advanced Research Institute for Science and*
Engineering, 17 Kikui-cho, Shinjuku-ku, Tokyo 162-0044, Japan
^{61}*Weizmann Institute, Rehovot 76100, Israel*
^{62}*Yonsei University, IPAP, Seoul 120-749, Korea*
(Dated: August 19, 2016)

Transverse momentum distributions and yields for $\pi^{\pm}$, $K^{\pm}$, p and $\overline{p}$ in $p+p$ collisions at $\sqrt{s} = 200$ and 62.4 GeV at midrapidity are measured by the PHENIX experiment at the Relativistic Heavy Ion Collider (RHIC). These data provide important baseline spectra for comparisons with identified particle spectra in heavy ion collisions at RHIC. We present the inverse slope parameter $T_{\rm inv}$, mean transverse momentum $\langle p_T \rangle$ and yield per unit rapidity dN/dy at each energy, and compare them to other measurements at different $\sqrt{s}$ in $p + p$ and $p + \overline{p}$ collisions. We also present the scaling properties such as m_T scaling, x_T scaling on the p_T spectra between different energies. To discuss the mechanism of the particle production in $p+p$ collisions, the measured spectra are compared to next-to-leading-order or next-to-leading-logarithmic perturbative quantum chromodynamics calculations.

PACS numbers: 25.75.Dw

I. INTRODUCTION

Single particle spectra of identified hadrons in high energy elementary collisions have attracted physicists for many decades due to their fundamental nature and simplicity. Particle production, in general, can be categorized into two different regimes depending on the transverse momentum of the hadrons. One is soft multiparticle production, dominant at low transverse momentum ($p_T \leq 2 \, \text{GeV}/c$), which corresponds to the ~ 1 fm scale of the nucleon radius described by constituent quarks. Another regime is hard-scattering particle production, evident at high transverse momentum ($p_T \geq 2 \, \text{GeV}/c$) due to the hard scattering of point-like current quarks, which corresponds to a very short distance scale ~ 0.1 fm [1] and contributes less than a few percent of the cross section for $\sqrt{s} \leq 200$ GeV. These two different regimes of particle production in $p + p$ collisions indicate that "elementary" $p + p$ collisions are actually rather complicated processes. It is interesting to know where the "soft-hard transition" happens, and its beam energy and particle species dependences, since they have not yet been fully understood.

In soft particle production, cosmic ray physicists observed in the 1950s that the average transverse momentum of secondary particles is limited to $\sim$0.5 GeV/c, independent of the primary energy [2, 3]. Cocconi, Koester and Perkins [4] then proposed the prescient empirical formula for the transverse momentum spectrum of meson production:

$$\frac{d\sigma}{p_T dp_T} = A e^{-6p_T}, \tag{1}$$

where p_T is the transverse momentum in GeV/c and $\langle p_T \rangle = 2/6 = 0.333$ GeV/c. The observation by Orear [5] that large angle $p + p$ elastic scattering measurements at AGS energies (10 to 30 GeV in incident energy) "can be fit by a single exponential in transverse momentum, and that this exponential is the very same exponential that describes the transverse momentum distribution of pions produced in nucleon-nucleon collisions", led to the interpretation [6] that particle production is "statistical" with Eq. 1 as a thermal Boltzmann spectrum, with $1/6 = 0.167$ GeV/c representing the "temperature" T at which the mesons or protons are emitted [7].

It was natural in a thermal scenario [8, 9] to represent the invariant cross section as a function of the rapidity (y) and the transverse mass ($m_T = \sqrt{p_T^2 + m^2}$) with a universal temperature parameter T. This description explained well the observed successively increasing $\langle p_T \rangle$ of π, K, p, Λ with increasing rest mass [10–12], and had the added advantage of explaining, by the simple factor $e^{-6(m_K - m_\pi)} \sim 12\%$, the low value of $\sim$10% observed for the K/π ratio at low p_T at ISR energies ($\sqrt{s} \sim$20–60 GeV) [13].

In 1964, the constituent quark model with SU(3) symmetry was introduced to explain the hadron flavor spectrum and the static properties of hadrons [14, 15]. Later on, a dynamical model was developed to calculate the flavor dependence of identified hadrons in soft multiparticle production [16], together with the inclusive reaction formalism [17–19]. These theoretical studies on the particle production mechanism showed that there was much to be learned by simply measuring a single particle spectrum, and it brought the study of identified inclusive single particle production into the mainstream of $p + p$ physics.

One of the controversial issues in understanding soft multi-particle production in the 1950's was whether more than one meson could be produced in a single nucleon-nucleon collision ("multiple production"), or whether the

*Deceased
†PHENIX Spokesperson: jacak@skipper.physics.sunysb.edu

multiple meson production observed in nucleon-nucleus ($p + A$) interactions was the result of several successive nucleon-nucleon collisions with each collision producing only a single meson ("plural production") [20]. The issue was decided when multiple meson production was first observed in 1954 at the Brookhaven Cosmotron in collisions between neutrons with energies up to 2.2 GeV and protons in a hydrogen filled cloud chamber [6, 21].

Then the observation of multi-particle production occurring not only in nucleon-nucleus ($p + A$) but also in nucleon-nucleon ($p + p$) collisions motivated Fermi and Landau to develop the statistical [22] and hydrodynamical [23] approach to multi-particle production. Belenkij and Landau observed that although the statistical model of Fermi is sufficient to describe the particle numbers in terms of only a temperature and a chemical potential, this model has to be extended to hydrodynamics, when particle spectra are considered. They also noted that the domain of the applicability of ideal relativistic hydrodynamics coincides with the domain of the applicability of thermodynamical models in high energy $p + p$ collisions [23].

On the other hand, understanding of the particle production by hard scattering partons has been advanced by the appearance of a rich body of data in $p + p$ collisions at the CERN-ISR [13, 24, 25] in the 1970s, followed by measurements at the Relativistic Heavy Ion Collider (RHIC) at $\sqrt{s} = 200$ [26–33] and 62.4 GeV [34] over the last decade. The hard scattering in $p + p$ collisions has been discovered by the observation of an unexpectedly large yield of particles with large transverse momentum and the phenomena of dijets at ISR [35]. These observations indicate that hard scattering process occurs between the quarks and gluons constituents (or partons) inside the nucleons. This scattering process can be described by the perturbative quantum chromodynamics (pQCD) because the strong coupling constant α_s of QCD becomes small (asymptotically free) for large momentum transfer (Q^2) parton-parton scatterings. After the initial high Q^2 parton-parton scatterings, these partons fragment into the high p_T hadrons or jets. In fact, at RHIC energies, single particle spectra of high p_T hadrons are well described by pQCD [30, 33, 34]. Furthermore, x_T ($= 2p_T/\sqrt{s}$), which is also inspired by pQCD, is known to be a good scaling variable of the particle production at high p_T at both ISR [36] and RHIC [34] energies, so that x_T scaling can be used to distinguish between the soft and hard particle productions.

Another important point of measurements in $p+p$ collisions is as a baseline for the heavy ion (A+A) data. The nuclear modification factor R_{AA}, for example, uses p_T spectra in $p + p$ collisions as a denominator, and those in A+A collisions (with the appropriate scaling of number of binary nucleon-nucleon collisions) as a numerator. In addition, p_T spectra in $p + p$ provide a reference of bulk properties of A+A collisions, such as the inverse slope parameter $T_{\rm inv}$, mean transverse momentum $\langle p_T \rangle$, and yield per unit rapidity dN/dy. These data in $p + p$ collisions can be treated as baseline values for the smallest A+A collisions.

In this paper, we present measurements of identified charged hadron p_T spectra for $\pi^{\pm}$, $K^{\pm}$, p and $\overline{p}$ at midrapidity in $p + p$ collisions at $\sqrt{s} = 200$ and 62.4 GeV from the PHENIX experiment. First, we compare the results of particle spectra at 200 GeV with those at 62.4 GeV as a function of p_T, m_T, and $m_T - m$ (where m is the rest mass). Second, the extracted values from p_T spectra, i.e. $T_{\rm inv}$, $\langle p_T \rangle$, and dN/dy, are compared between the two beam energies. For the systematic study of particle production as a function of $\sqrt{s}$ the data are further compared to measurements in $p + p$ and $p + \overline{p}$ collisions at the CERN-ISR and FNAL-Tevatron colliders.

From these measurements, we discuss the following key issues:

hard scattering particle production – The data are compared with the results of perturbative quantum chromodynamics (pQCD) calculations.

transition from soft to hard physics – Since the p_T regions presented in this paper can cover the region where the soft-hard transition occurs, the scaling properties in m_T and x_T with their beam energy and particle species dependences are shown.

comparisons with heavy-ion data as a baseline measurement – Some of the data in $p + p$ are compared with the existing data in Au+Au [37].

The paper is organized as follows: Section II describes the PHENIX detector as it was used in this measurement. Section III discusses the analysis details, including data sets, event selection, track selection, particle identification, corrections applied to the data, and systematic uncertainties. Section IV gives the experimental results for p_T spectra for identified charged particles, particle ratios, m_T scaling, the excitation function of observables (such as $T_{\rm inv}$, $\langle p_T \rangle$, and dN/dy), and R_{AA}. Section V compares the results with next-to-leading-order (NLO) and next-to-leading-log (NLL) pQCD calculations, and discuss soft and hard particle production, and the transition between them. Section VI gives the summary and conclusions.

II. EXPERIMENTAL SETUP

The PHENIX experiment is designed to perform a broad study of A+A, $d + A$, and $p + p$ collisions to investigate nuclear matter under extreme conditions, as well as to measure the spin structure of the nucleon. It is composed of two central arms (called east and west arm, respectively), two forward muon arms, and global detectors, as shown in Fig. 1. The central arms are designed to detect electrons, photons and charged hadrons in the pseudorapidity range $|\eta| < 0.35$. The global detectors measure the start time, collision vertex, and charged
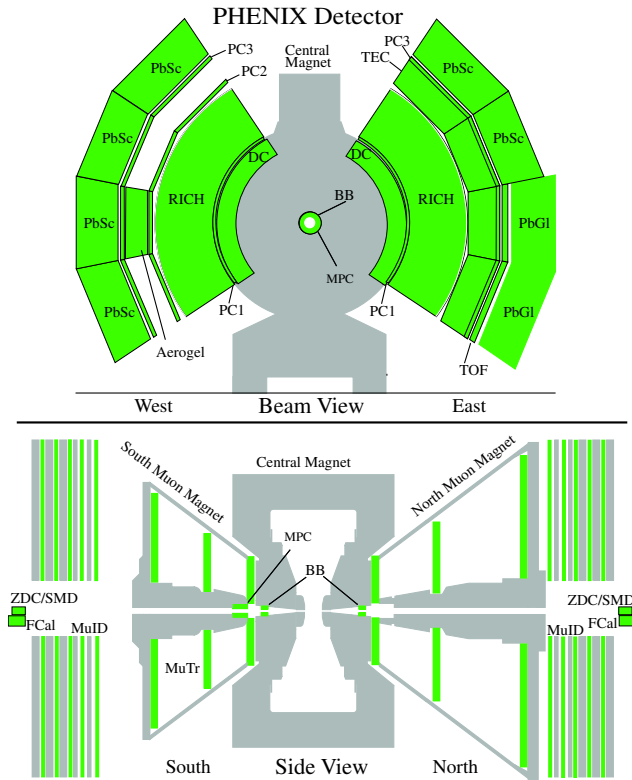
FIG. 1: (color online) The PHENIX detector configuration for RHIC Run-6 data taking period. The beam-beam counter (BBC) is labeled as BB on the figure.

hadron multiplicity of the interactions in the forward pseudorapidity region. The following sections describe those parts of the detector that are used in the present analysis. A detailed description of the complete set of detectors can be found elsewhere [38–42].

The beam-beam counters (BBC) [41] determine the start time information for time-of-flight measurements and the collision vertex point, as well as providing the main collision trigger. The two BBCs are located at 1.44 m from the nominal interaction point along the beam line on each side. Each BBC comprises 64 Čerenkov telescopes, arranged radially around the beam line. The BBCs measure the number of charged particles in the pseudorapidity region $3.0 < |\eta| < 3.9$.

Charged particle tracks are reconstructed using the central arm spectrometers [42]. The east arm spectrometer of the PHENIX detector contains the following subsystems used in this analysis: drift chamber (DC), pad chamber (PC) and time of flight (TOF). The magnetic field for the central arm spectrometers is supplied by the central magnet [39] that provides an axial field parallel to the beam around the collision vertex.

The drift chambers are the closest tracking detectors to the beam line, located at a radial distance of 2.2 m (ge-

ometric center, same for other detectors). They measure charged particle trajectories in the azimuthal direction to determine the transverse momentum of each particle. By combining the polar angle information from the first layer of PC, as described below, with the transverse momentum, the total momentum p is determined. The momentum resolution in $p+p$ collisions is $\delta p/p \simeq 0.7\% \oplus 1.0\% \times p$ (GeV/c), where the first term is due to the multiple scattering before DC and the second term is the angular resolution of the DC. The absolute momentum scale is known as $\pm$ 0.7% rms from the reconstructed proton mass using TOF.

The pad chambers are multi-wire proportional chambers that form three separate layers of the central tracking system. The first layer (PC1) is located at the radial outer edge of each drift chamber at a distance of 2.49 m, while the third layer is at 4.98 m from the interaction point. The second layer is located at a radial distance of 4.19 m in the west arm only. PC1 and DC, along with the vertex position measured by BBC, are used in the global track reconstruction to determine the polar angle of each charged track.

The time-of-flight detector serves as the primary particle identification device for charged hadrons by measuring the stop time. The start time is given by BBC. TOF is located at a radial distance of 5.06 m from the interaction point in the east central arm. This contains 960 scintillator slats oriented along the azimuthal direction. It is designed to cover $|\eta| < 0.35$ and $\Delta\phi = 45^o$ in azimuthal angle. The intrinsic timing resolution is $\sigma \simeq 115$ ps, which in combination with the BBC timing resolution of 60 ps, allows for a 2.6σ π/K separation at $p_T \simeq 2.5$ GeV/c, and K/p separation out to $p_T = 4.5$ GeV/c, using an asymmetric particle-identification (PID) cut, as described below.

III. DATA ANALYSIS

The two RHIC data sets analyzed are 2005 data for $p + p$ collisions at $\sqrt{s} =$ 200 GeV and 2006 data for $p + p$ collisions at $\sqrt{s} = 62.4$ GeV. Each data set was analyzed separately by taking into account the different run conditions and accelerator performance. In this section, we explain the event selection, track reconstruction, particle identification, and corrections to obtain the p_T spectra. The event normalization and systematic uncertainties are also presented.

A. Event selection

We use the PHENIX minimum bias trigger events, which are determined by a coincidence between north and south BBC signals, requiring at least one hit on both sides of BBCs. Due to the limited acceptance, approximately only half of the $p + p$ inelastic cross section can be measured by BBC. The PHENIX minimum bias data,

triggered by BBC in $p+p$ collisions within a vertex cut of ± 30 cm, include $\sigma_{BBC} = 23.0 \pm 2.2$ mb at $\sqrt{s} = 200$ GeV and $\sigma_{BBC} = 13.7 \pm 1.5$ mb at $\sqrt{s} = 62.4$ GeV (see Section III E). We analyze 9.2×10^8 minimum bias events for the 2005 $p+p$ data at $\sqrt{s} = 200$ GeV, which is more than 30 times larger than the 2003 data set [26] and 2.14×10^8 times larger than the minimum bias events for the 2006 data at $\sqrt{s} = 62.4$ GeV.

B. Track reconstruction and particle identification

As in previous publications [37, 43], charged particle tracks are reconstructed by DC based on a combinatorial Hough transform, which gives the angle of the track in the main bend plane. PC1 is used to measure the position of the hit in the longitudinal direction along the beam axis. When combined with the location of the collision vertex along the beam axis, the PC1 hit gives the polar angle of the track. Only tracks with valid information from both DC and PC1 are used in the analysis. To associate a track with a hit on TOF, the track is projected to its expected hit location on TOF. We require tracks to have a hit on TOF within $\pm 2\sigma$ of the expected hit location in both the azimuthal and beam directions. The track reconstruction efficiency is approximately 98% in $p + p$ collisions. Finally, a cut on the energy loss in the TOF scintillator is applied to each track. This β-dependent energy loss cut is based on a parameterization of the Bethe-Bloch formula. The flight path length is calculated from a fit to the reconstructed track trajectory in the magnetic field. The background due to random association of DC/PC1 tracks with TOF hits is reduced to a negligible level when the mass cut used for particle identification is applied.

Charged particles are identified using the combination of three measurements: time-of-flight from the BBC and TOF, momentum from the DC, and flight-path length from the collision vertex point to the TOF hit position. The square of mass is derived from

$$m^2 = \frac{p^2}{c^2}\left[\left(\frac{t_{tof}}{L/c}\right)^2 - 1\right], \qquad (2)$$

where p is the momentum, t_{tof} is the time of flight, L is the flight path length, and c is the speed of light. The charged particle identification is performed using cuts in m^2 and momentum space. In Fig. 2, a plot of momentum multiplied by charge versus m^2 is shown together with applied PID cuts as solid curves. We use 2σ standard deviation PID cuts in m^2 and momentum space for each particle species. The PID cut is based on a parameterization of the measured m^2 width as a function of momentum

$$\sigma_{m^2}^2 = \frac{\sigma_\alpha^2}{K_1^2}(4m^4p^2) + \frac{\sigma_{ms}^2}{K_1^2}\left[4m^4\left(1 + \frac{m^2}{p^2}\right)\right]$$
$$+ \frac{\sigma_t^2 c^2}{L^2}\left[4p^2\left(m^2 + p^2\right)\right], \qquad (3)$$

where σ_α is the angular resolution, σ_{ms} is the multiple scattering term, σ_t is the overall time-of-flight resolution, m is the centroid of m^2 distribution for each particle species, and K_1 is the magnetic field integral constant term of 101 mrad·GeV. The parameters for PID are $\sigma_\alpha = 0.99$ mrad, $\sigma_{ms} = 1.02$ mrad·GeV, and $\sigma_t = 130$ ps. For pion identification above 2 GeV/c, we apply an asymmetric PID cut to reduce kaon contamination of pions. As shown by the lines in Fig. 2, the overlap regions which are within the 2σ cuts for both pions and kaons are excluded. The lower momentum cut-offs are 0.3 GeV/c for pions, 0.4 GeV/c for kaons, and 0.5 GeV/c for protons and antiprotons. The lower momentum cut-off value for p and $\overline{p}$ is larger than for pions and kaons due to the larger energy loss effect.

For kaons, the upper momentum cut-off is 2 GeV/c since the $\pi + p$ contamination level for kaons is $\approx 8\%$ at that momentum. The upper momentum cut-off for pions is $p_T = 3$ GeV/c where the $K + p$ contamination reaches $\approx 3\%$. Electron (positron) and decay muon background at very low p_T (< 0.3 GeV/c) are well separated from the pion mass-squared peak. For protons the upper momentum cut-off is set at 4.5 GeV/c. For protons and antiprotons an additional cut, $m^2 > 0.6(\text{GeV}/c^2)^2$, is introduced to reduce the contamination. The contamination background on each particle species is subtracted statistically after applying these PID cuts.
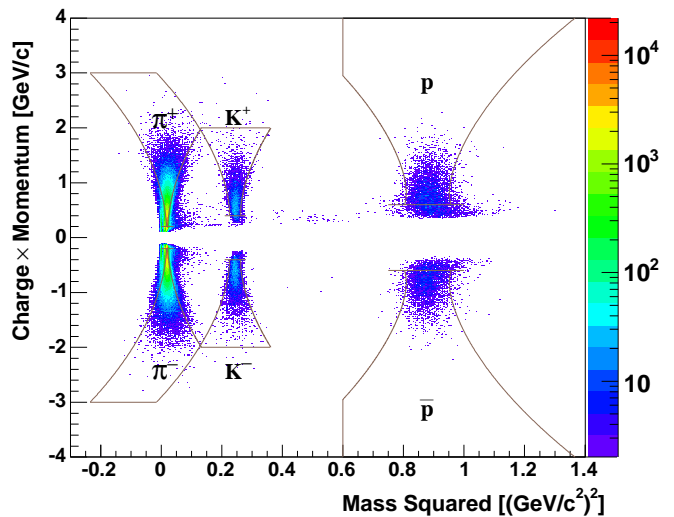

FIG. 2: (color online) Momentum multiplied by charge versus mass squared distribution in $p+p$ collisions at $\sqrt{s} = 62.4$ GeV. The lines indicate the PID cut boundaries (2σ) for pions, kaons, and protons (antiprotons) from left to right, respectively.

C. Efficiency corrections

We use the PHENIX-integrated-simulation application, which is a GEANT [44] based Monte Carlo (MC)

simulation program of the PHENIX detector, to correct for geometrical acceptance, reconstruction efficiency, in-flight decay for π and K, multiple scattering effect, and nuclear interactions with materials in the detector (including $\overline{p}$ absorption). Single particle tracks are passed from GEANT to the PHENIX event reconstruction software [43]. In this simulation, the BBC, DC, and TOF detector responses are tuned to match the real data. For example, dead areas of DC and TOF are included, and momentum and time-of-flight resolutions are tuned. The track association to TOF in both azimuth and along the beam axis as a function of momentum and the PID cut boundaries are parameterized to match the real data. A fiducial cut is applied to choose identical active areas on TOF in both the simulation and data.

We generate 1×10^7 single particle events for each particle species ($\pi^\pm$, $K^\pm$, p and $\overline{p}$) with flat p_T distributions for high p_T (2–4 GeV/c for pions and kaons, 2–8 GeV/c for p and $\overline{p}$) with enhancement at low p_T (< 2 GeV/c). Weighting functions to the p_T distributions are also used to check the effect of steepness, which is less than $\sim 1\%$ level on the final yields in the measured p_T range. The rapidity range is set to be wider than the PHENIX acceptance, i.e. flat in $-0.6 < y < 0.6$ ($\Delta y = 1.2$) to deal with particles coming from outside (the denominator of Eq. 4 is weighted with a factor $1/\Delta y = 1/1.2$ in order to normalize the yield for unit rapidity). The efficiencies are determined in each p_T bin by dividing the reconstructed output by the generated input as expressed as follows:

$$\epsilon(p_T) = \frac{\text{\# of reconstructed MC tracks}}{\text{\# of generated MC tracks}}. \quad (4)$$

The resulting correction factors $C_{\text{eff}}(p_T)$ ($= 1/\epsilon(p_T)$) is multiplied to the raw p_T spectra for each p_T bin and for each individual particle species (see Section III G).

D. Feed-down corrections

The proton and antiproton p_T spectra are corrected for feed-down from weak decays of hyperons. The detailed procedure of the feed-down correction can be found in [26]. We include the following decay modes: $\Lambda \to p\pi^-$, $\Sigma^+ \to p\pi^0$, and Λ production from Σ^0, Ξ^0, Ξ^-. The feed-down contributions for antiproton yields are also estimated using the above decay modes for antiparticles.

In order to estimate the fractions of protons and antiprotons from weak decays of hyperons in the measured proton and antiproton p_T spectra, we use three input Λ and $\overline{\Lambda}$ p_T spectra:

1. measured Λ and $\overline{\Lambda}$ p_T spectra in PHENIX in $p + p$ collisions at $\sqrt{s} = 200$ and 62.4 GeV,

2. measured p ($\overline{p}$) distributions scaled with measured Λ ($\overline{\Lambda}$) distributions [31], and

3. measured p ($\overline{p}$) distributions scaled with ISR Λ ($\overline{\Lambda}$) distributions [25].

Using each input above, proton and antiproton spectra from weak decays are calculated by using Monte Carlo simulation to take into account decay kinematics, the PHENIX track reconstruction efficiency and experimental acceptance. Then systematic uncertainties are evaluated from different Λ and $\overline{\Lambda}$ spectra inputs. The resulting uncertainties on the final proton and antiproton spectra are of the order of 20–30% at $p_T = 0.6$ GeV/c and 2–5% at $p_T = 4$ GeV/c. The fractional contribution of the feed-down protons (antiprotons) to the total measured proton (antiproton) spectra, $\delta_{\text{feed}}(p_T)$, is approximately 10–20 (5–15) % at $p_T = 4$ GeV/c for 200 GeV $p + p$ (62.4 GeV $p + p$) and it shows an increase at lower p_T as shown in Fig. 3. The correction factor for the feed-down correction can be expressed as: $C_{\text{feed}}(p_T) = 1 - \delta_{\text{feed}}(p_T)$, which is multiplied to the raw p_T spectra (see Section III G).

The feed-down correction for protons is different from that for antiprotons in 62.4 GeV, because of the difference in Λ/p and $\overline{\Lambda}/\overline{p}$ ratio at this beam energy. At 62.4 GeV, Λ/p ratio is 0.2 while $\overline{\Lambda}/\overline{p}$ ratio is 0.4 [25], so that the feed-down contribution for antiprotons is bigger than that for protons. At 200 GeV, these two ratios are almost same [31], therefore the feed-down corrections for p and $\overline{p}$ become identical.

E. Cross section normalization

The BBC counter serves a dual function as both the minimum bias trigger and the calibrated luminosity monitor. The luminosity $\mathcal{L}$ is defined as the interaction rate for a given cross section: $dN/dt = \mathcal{L}\sigma$ and the total number of events for a given cross section is

$$N = \sigma \times \int \mathcal{L}dt, \quad (5)$$

where $\int \mathcal{L}dt$ is the integrated luminosity. To connect the number of minimum bias triggered events and the integrated luminosity, σ_{BBC} is introduced where $1/\sigma_{\text{BBC}}$ corresponds to the integrated luminosity per minimum bias triggered event (Eq. 6).

$$N_{\text{BBC}} = \sigma_{\text{BBC}} \times \int \mathcal{L}dt, \quad (6)$$

where N_{BBC} is the number of minimum bias events and $\int \mathcal{L}dt$ is the corresponding integrated luminosity. σ_{BBC} is measured by a Van der Meer scan method (Vernier scan) in PHENIX [34, 45].

Vernier scans were performed for $\sqrt{s} = 200$ and 62.4 GeV data sets. The obtained σ_{BBC} are 23.0 ± 2.2 mb and 13.7 ± 1.5 mb for $\sqrt{s} = 200$ and 62.4 GeV respectively. The quoted uncertainty is a systematic uncertainty. These numbers were reported in our measurements of π^0 production [30, 34].
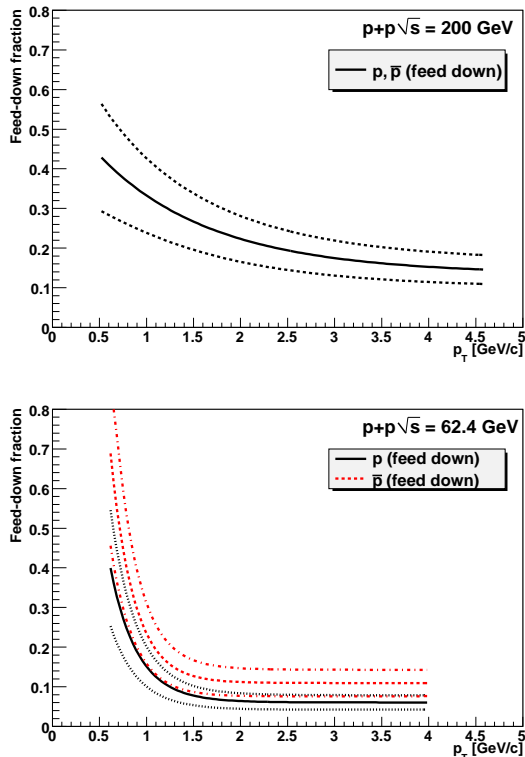
trigger bias. We use this p_T dependent trigger bias correction for charged hadrons, by using fitted coefficients of a second order polynomial, as shown in Fig. 4.

With those values, the invariant yield per BBC trigger count (Y/N_{BBC}) is related to the invariant cross section (σ) using

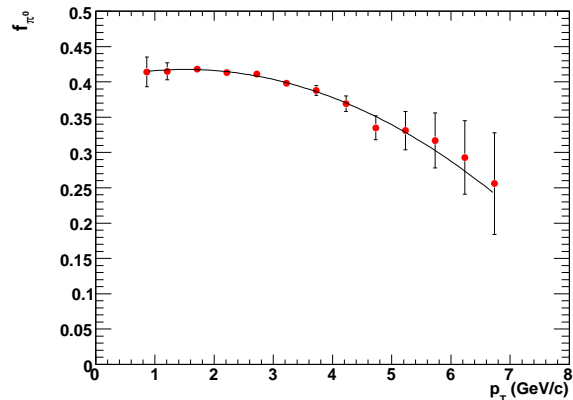$$\sigma = (Y/N_{\text{BBC}}) \times (\sigma_{\text{BBC}}/\epsilon_{\text{bias}}). \qquad (7)$$

FIG. 4: (color online) Fraction of the inclusive π^0 yield which satisfied the BBC trigger condition in 62.4 GeV $p + p$. Data points are from Fig. 1 of [34].

FIG. 3: (color online) Fraction of feed-down protons and antiprotons as a function of p_T with systematic uncertainties. Top: 200 GeV $p+p$ (positive and negative functions are common). Bottom: 62.4 GeV $p + p$.

Since the minimum bias trigger registers only half of the $p + p$ inelastic cross section, it is expected that there is a trigger bias against particles in the central spectrometers. This was checked with π^0's in the electromagnetic calorimeter with high p_T photon triggered events, and with charged tracks in accelerator's beam crossing (clock) triggered events. The trigger bias ϵ_{bias} determined from the ratio (f_{π^0}) of the number of π^0 in the high p_T photon triggered sample with and without the BBC trigger requirement[34]. We assume ϵ_{bias} is process dependent and so that it is measured as $\epsilon_{\text{bias}} = f_{\pi^0}$. This ratio, f_{π^0}, is 0.79 ± 0.02 independent of the transverse momentum for $\sqrt{s} = 200$ GeV. At 62.4 GeV, the trigger bias was found to be transverse momentum dependent [34]. Fig. 4 shows that the trigger bias f_{π^0}, and f_{π^0} is $\approx 40\%$ up to $p_T \approx 3$ GeV/c, and monotonically decreases to 25% at $p_T \approx 7$ GeV/c. As described in the previous PHENIX publication [34], this decrease can be understood by the fact that most of the energy is used for the production of high-energy jets which contain the measured high p_T π^0 and charged hadrons, and there is not enough energy left to produce particles for $\sqrt{s} = 62.4$ GeV $p+p$ collisions at the forward rapidity ($3.0 < |\eta| < 3.9$) where the BBC is located. This drop can be seen only for 62.4 GeV data. Also we assume no particle species dependence for this

F. Systematic uncertainties

In order to estimate the systematic uncertainties, the p_T spectra with slightly different analysis cuts from what we use for the final results are prepared, and these spectra are compared to those with the standard analysis cuts. We checked the following analysis cuts: (1) fiducial, (2) track association windows, and (3) PID.

For each spectrum with modified cuts, the same changes in the cuts are made in the Monte Carlo simulation. The fully corrected spectra with different cut conditions are divided by the spectra with the baseline cut condition, resulting in uncertainties associated with each cut condition as a function of p_T. The obtained uncertainties are added in quadrature. Tables I and II show the systematic uncertainties on p_T spectra for each data set. There are three categories of systematic uncertainty: Type A is a point-to-point error uncorrelated between p_T bins, type B is p_T correlated, where all points move in the same direction but not by the same factor, while in type C all points move by the same factor independent of p_T [46]. In this study, the systematic uncertainties on feed-down correction and PID contamination correction are Type B, other systematic uncertainties on applied analysis cuts are Type C. There are two types of the PID-related uncertainties. One is the systematic uncertainty of the yield extraction, which is evaluated by

TABLE I: Systematic uncertainties on the p_T spectra for $\sqrt{s} = 200$ GeV $p + p$ given in percent. The number in parenthesis includes the p_T dependence of the uncertainties for PID cut, feed-down correction, PID contamination correction.

Source	π^+	π^-	K^+	K^-	p	$\overline{p}$
Fiducial Cut	5	5	4	5	4	5
Track Matching	4	4	5	4	4	4
PID Cut	3	3	2	2	2–8	2–10
Efficiency Correction	2	2	2	2	2	2
Feed-down Correction	-	-	-	-	4–25	4–25
PID Contamination	-	-	-	-	0–2	0–2
Total	7	7	7	7	6 (8–25)	7 (9–25)

TABLE II: Systematic uncertainties on the p_T spectra for $\sqrt{s} = 62.4$ GeV $p + p$ given in percent. The number in parenthesis includes the p_T dependence of the uncertainties for feed-down correction, PID contamination correction.

Source	π^+	π^-	K^+	K^-	p	$\overline{p}$
Fiducial Cut	6	5	6	5	7	5
Track Matching	2	2	3	3	3	3
PID Cut	2	2	3	3	4	4
Efficiency Correction	2	2	2	2	2	2
Feed-down Correction	-	-	-	-	1–16	3–50
PID Contamination	-	-	0–5	0–5	-	-
Total	7	6	7	7	9 (9–18)	7 (8–50)

changing the PID boundary in m^2 vs momentum plane. The other is the systematic uncertainty of the particle contamination, which is evaluated by using the contamination fraction. The fraction is estimated by fitting m^2 distributions on each p_T slice under the several conditions as follows: (1) fixed parameters for p and $\overline{p}$ mass centroid and width, (2) p and $\overline{p}$ mass centroid free with fixed mass width, (3) p and $\overline{p}$ mass width free with fixed mass centroid.

The systematic uncertainty on the BBC cross section is 9.7% and 11% for $\sqrt{s} = 200$ and 62.4 GeV respectively. The systematic uncertainty on the trigger bias is 3% and 1–5% for $\sqrt{s} = 200$ and 62.4 GeV respectively (see Section III E). These uncertainties on normalization (Type C) are not included in Tables I and II. All the figures and tables including the tables in Appendix A do not include the normalization uncertainties, unless explicitly noted.

G. Invariant cross section

The differential invariant cross section is determined as

$$E\frac{d^3\sigma}{dp^3} = \frac{1}{2\pi p_T}\frac{\sigma_{\mathrm{BBC}}}{N_{\mathrm{BBC}}C_{\mathrm{bias}}^{\mathrm{BBC}}(p_T)}C_{\mathrm{eff}}(p_T)C_{\mathrm{feed}}(p_T)\frac{d^2N}{dp_T dy}, \tag{8}$$

where σ is the cross section, p_T is transverse momentum, and y is rapidity, N_{BBC} is the number of minimum bias events, σ_{BBC} is the minimum bias cross section measured by BBC, $C_{\mathrm{eff}}(p_T)$ is the acceptance correction factor including detector efficiency, $C_{\mathrm{bias}}^{\mathrm{BBC}}(p_T)$ is the trigger bias, $C_{\mathrm{feed}}(p_T)$ is the feed-down correction factor only for protons and antiprotons, and N is the number of measured tracks.

IV. RESULTS

In this section, we show the transverse momentum distributions and yields for $\pi^\pm$, $K^\pm$, p and $\overline{p}$ in $p + p$ collisions at $\sqrt{s} = 200$ and 62.4 GeV at midrapidity mea-

sured by the PHENIX experiment. We also present the transverse mass (m_T) spectra, the inverse slope parameter T_{inv}, mean transverse momentum $\langle p_T \rangle$, yield per unit rapidity dN/dy, and particle ratios at each energy, and compare them to other measurements at different $\sqrt{s}$ in $p + p$ and $p + \overline{p}$ collisions. The measured T_{inv}, $\langle p_T \rangle$, and dN/dy in $p + p$ 200 GeV are also compared with those in published results in Au+Au at 200 GeV. The nuclear modification factor R_{AA} for 200 GeV Au+Au using the present study in $p + p$ 200 GeV are also presented.

A. p_T spectra

Figure 5 shows transverse momentum spectra for $\pi^\pm$, $K^\pm$, p, and $\overline{p}$ in 200 and 62.4 GeV $p + p$ collisions. Feed-down correction for weak decays is applied for p and $\overline{p}$, and the same correction factors are consistently used for all figures through Section IV unless otherwise specified. The systematic uncertainty on the BBC cross section is 9.7% and 11% for $\sqrt{s} = 200$ and 62.4 GeV respectively. Each of p_T spectra is fitted with an exponential functional form:

$$\frac{1}{2\pi p_T}\frac{d^2\sigma}{dy dp_T} = A\exp\left(-\frac{p_T}{T}\right) \tag{9}$$

where A is a normalization factor and T is an inverse slope parameter for p_T. The fitting parameters and χ^2/NDF by using Eq. 9 for $\pi^\pm$, $K^\pm$, p, and $\overline{p}$ in 200 and 62.4 GeV $p + p$ collisions, are tabulated in Table III. The fitting range is fixed as $p_T = 0.5$–1.5 GeV/c for $\pi^\pm$, 0.6–2.0 GeV/c for $K^\pm$, and 0.8–2.5 GeV/c for p, $\overline{p}$ at both collision energies.

Figure 5 shows that pions, protons, and antiprotons exhibit an exponential spectral shape at low p_T and a power-law shape at high p_T, while kaons are exponential in the measured p_T range. The transition from exponential to power-law can be better seen at $p_T \sim 2$ GeV/c for pions, and at $p_T \sim 3$ GeV/c for protons and antiprotons at both energies. The fractions of soft and hard components gradually change in the transition region.
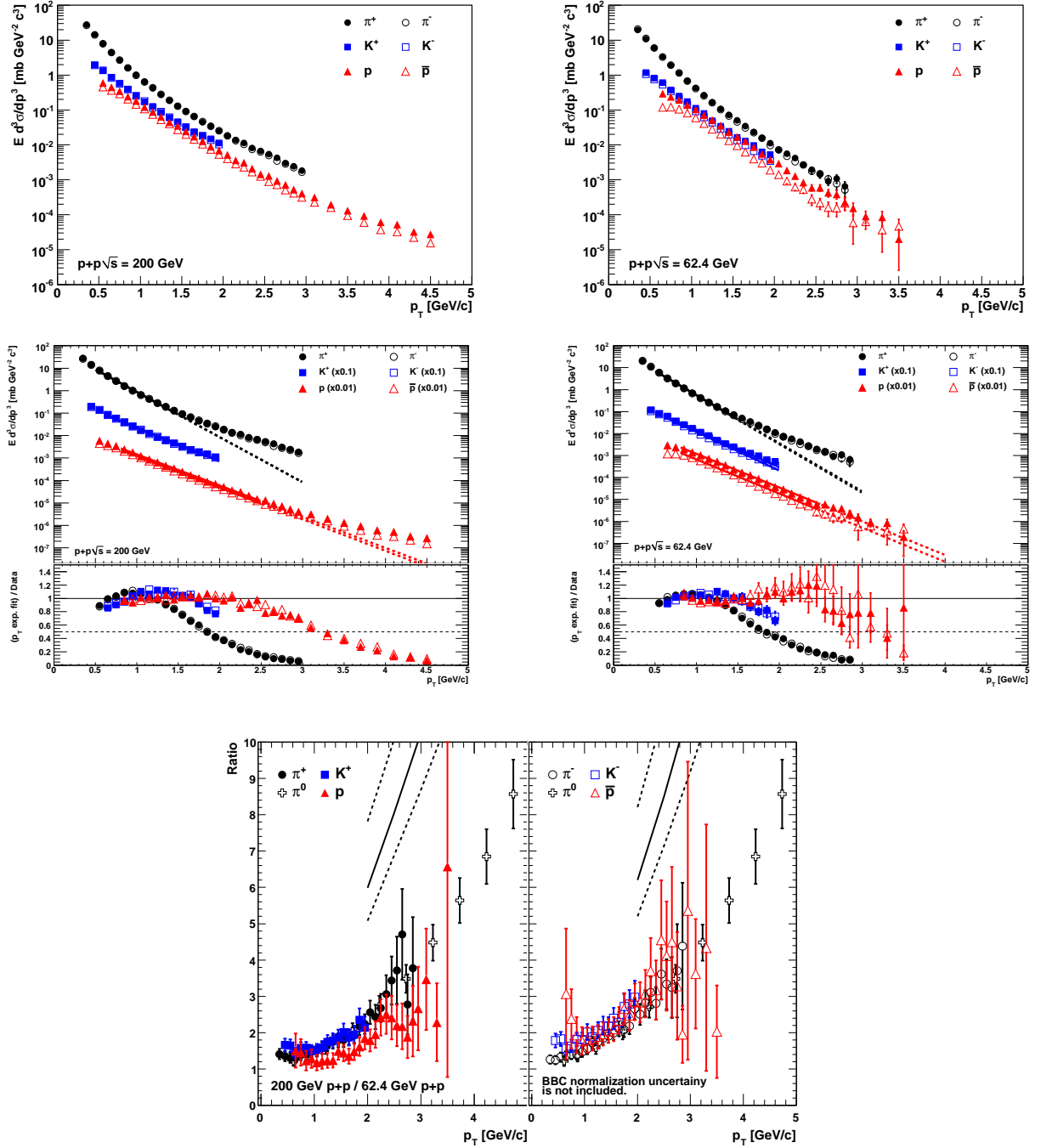
FIG. 5: (color online) (top, middle) Transverse momentum distributions for $\pi^{\pm}$, $K^{\pm}$, p, and $\overline{p}$ in $p + p$ collisions at $\sqrt{s}$ = (left) 200 and (right) 62.4 GeV at midrapidity. Only statistical uncertainties are shown. (middle plots) Each spectrum is fitted with an exponential function. (lower panels of middle plots) Ratio of the exponential fit to data for each particle species. (bottom) Ratios of p_T spectra for $\pi^{\pm}$, π^0 [30, 34], $K^{\pm}$, p, and $\overline{p}$ in 200 GeV $p + p$ collisions to those in 62.4 GeV $p + p$ collisions. Statistical and systematic uncertainties are combined in quadrature. The trigger cross section uncertainty is not included. The lines represent the NLO pQCD calculations (DSS fragmentation function) for pions with different factorization, fragmentation, and renormalization scales (which are equal) [47].

Ratios of the p_T spectra at 200 GeV to those at 62.4 GeV are shown in the bottom plot of Fig. 5. The left panel shows the ratios for positively charged particles, and the right panel is those for the negatively charged

particles. The data for neutral pions [30, 34] are also shown on both panels. The ratios show a clear increase as a function of p_T for all the ratios. Since hard scattering is expected to be the dominant particle production pro-
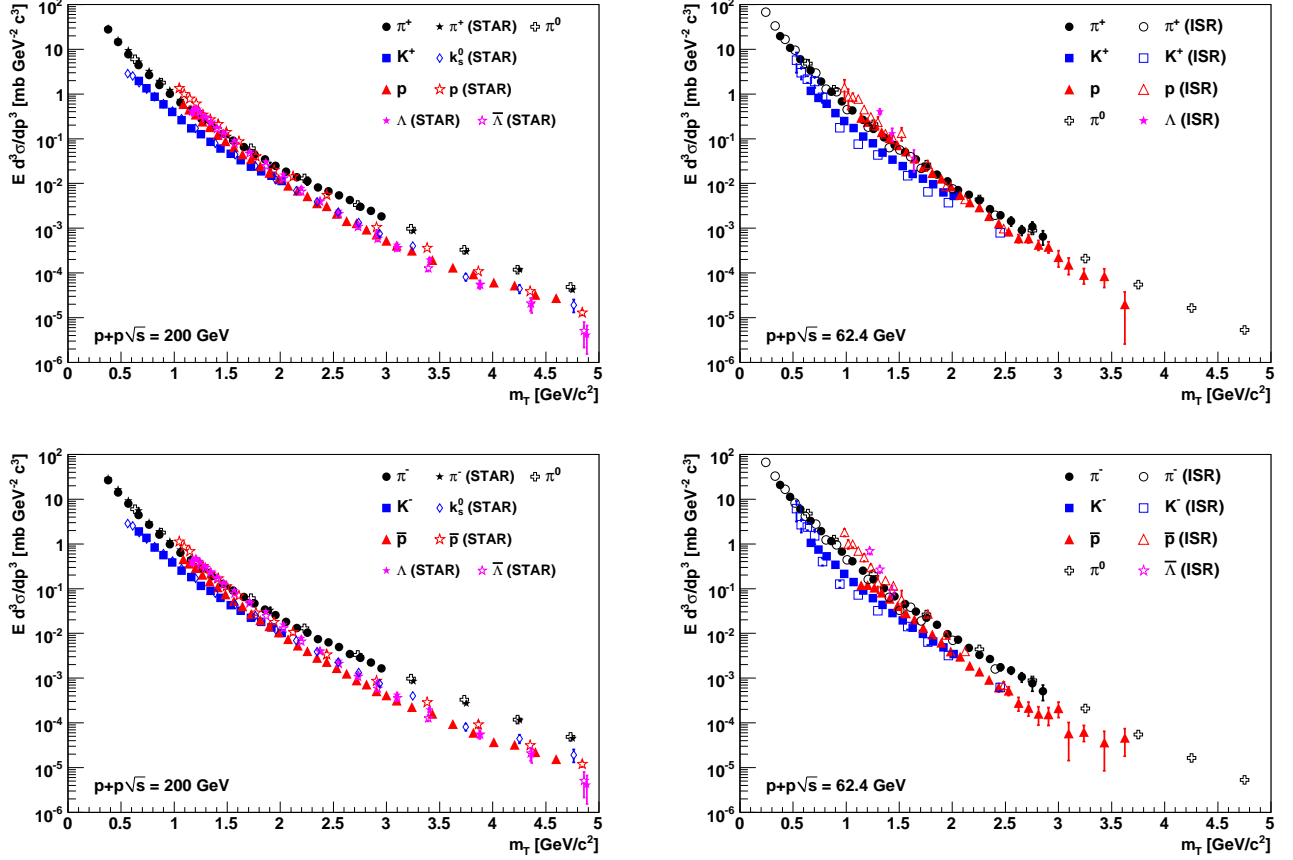
FIG. 6: (color online) Transverse mass distributions for $\pi^{\pm}$, π^{0}, $K^{\pm}$, p, and $\overline{p}$ in $p + p$ collisions at $\sqrt{s} =$ (left) 200 and (right) 62.4 GeV at midrapidity for (upper) positive and (lower) negative hadrons. Only statistical uncertainties are shown. The references for STAR data are $\pi^{\pm}$, p, $\overline{p}$ [33] and K_s^0, Λ, $\overline{\Lambda}$ [31]. The references for ISR data are $\pi^{\pm}$, $K^{\pm}$, p, $\overline{p}$ [13] and Λ, $\overline{\Lambda}$ [25].

cess at high p_T, this strong p_T dependence indicates two features: (1) spectral shape is harder for 200 GeV compared to those for 62.4 GeV, and (2) a universal shape for all particle species up to $p_T = 2$–3 GeV/c. In the same figure, the results from NLO pQCD calculations with DSS fragmentation function [47] for pions with different factorization, fragmentation, and renormalization scales (which are equal) are also shown. The agreement is relatively poor, due to the disagreement between the NLO pQCD calculation with DSS fragmentation function and measurement for pions at $\sqrt{s} = 62.4$ GeV. As we will discuss in detail in Section V C, it is found that NLL pQCD gives a better description of the data for $p+p$ at 62.4 GeV.

Please note that each line in pQCD is calculated for each μ ($= p_T/2$, p_T, $2p_T$) value. The hard scale resides in the hard scattering, which is expected to be the same regardless of hadron species. The theoretical uncertainty in the ratio of NLO (200 GeV / 62.4 GeV) significantly cancels. The same comparison of ratio for NLL cannot be made due to the unreliability of resummation in NLL pQCD at 200 GeV in the low p_T region [47].

B. m_T spectra

In $p + p(\overline{p})$ collisions at high energies, the transverse mass (m_T) spectra of identified hadrons show a universal scaling behavior, and this fact is known as m_T scaling. In order to check the m_T scaling and to gain a further insight on the particle production mechanism especially at high p_T at RHIC energies, transverse mass spectra in 200 and 62.4 GeV $p+p$ collisions are shown in Fig. 6. The data for $\pi^{\pm}$, $K^{\pm}$, p, and $\overline{p}$ in 200 and 62.4 GeV are from this study. The π^0 spectra are taken from the PHENIX measurements [30, 34]. From the STAR experiment, $\pi^{\pm}$, p, and $\overline{p}$ spectra in 200 GeV $p + p$ are taken from [33], and K_s^0, Λ, and $\overline{\Lambda}$ spectra in 200 GeV $p + p$ are taken from [31]. The $\pi^{\pm}$, $K^{\pm}$, p, $\overline{p}$ spectra in 63 GeV $p + p$ are from [13], and Λ, $\overline{\Lambda}$ spectra in 63 GeV $p + p$ are from the ISR experiment [25]. For both energies one can see "almost" the same spectral shape for all particle species. However, this scaling is not perfect, because it is violated by the yields that are different for each particle species. In order to see the approximate scaling behavior and its violation more clearly, one needs to introduce certain factors, that normalize these yields to make them
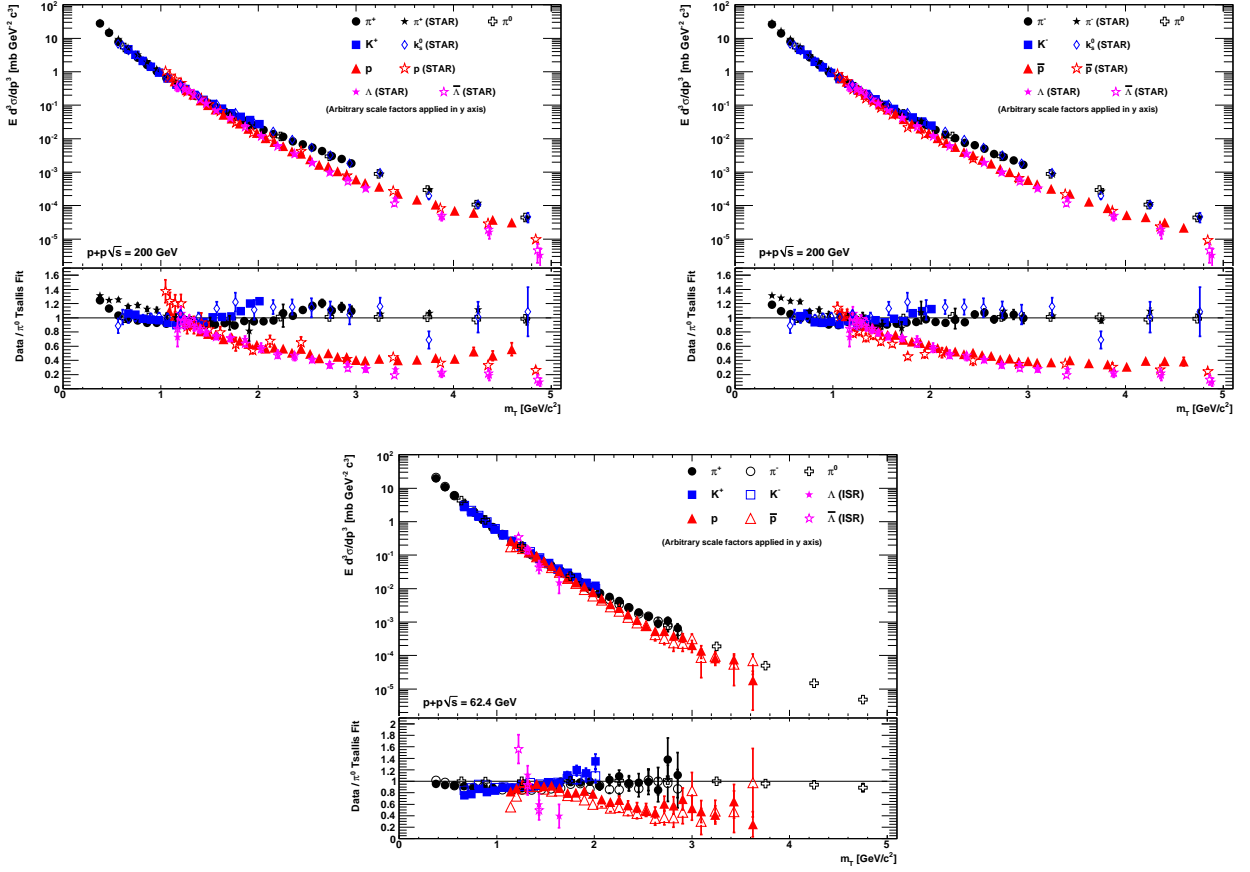
FIG. 7: (color online) Scaled transverse mass distributions for $\pi^{\pm}$, π^0, $K^{\pm}$, p, and $\overline{p}$ in $p + p$ collisions at $\sqrt{s} =$ (upper) 200 and (lower) 62.4 GeV at midrapidity for (upper left) positive, (upper right) negative, and (lower) $\pm$ hadrons. Only statistical uncertainties are shown. (upper) The STAR spectra for K_s^0, Λ, $\overline{\Lambda}$ are from [31]. (lower) The ISR spectra for Λ, $\overline{\Lambda}$ are from [25]. Arbitrary scaling factors are applied to match the yield of other particles to that of charged pions in the range of $m_T = 1.0$–1.5 GeV/c^2. The lower panels of each plot show the ratio to π^0 Tsallis fit.

coincide at a certain value of m_T.

Figure 7 shows the m_T spectra with such scaling factors implemented. These normalization scaling factors are determined to match the yield of each particle species to that of charged pions in the range of $m_T = 1.0$–1.5 GeV/c^2, i.e. factors which scale the normalization (vertical axis) as in the legends of Fig. 7. These scaling factors are tabulated in Table IV. The bottom panels on the plots in Fig. 7 are the ratio of data to the fitting result using Tsallis function for π^0 data in 200 GeV [30] and 62.4 GeV [34]. Above $m_T > 1.5$ GeV/c^2, these figures indicate a clear separation between meson and baryon spectra. The meson spectra are apparently harder than the baryon spectra in this representation. This effect can be seen more clearly on the $\sqrt{s} = 200$ GeV dataset, than on data measured at 62.4 GeV. Such a baryon-meson splitting in m_T spectra has been reported by the STAR experiment in $p+p$ collisions at $\sqrt{s} = 200$ GeV [31]. That paper argued for a given jet energy, mesons might be produced with higher transverse momentum than baryons, because meson production in jet fragmentation requires

only a (quark, antiquark) pair, while baryon production requires a (diquark, antidiquark) pair.

However, such a rescaling along the vertical axis is arbitrary. Since it is known that the shapes of the power-law tail for different particle species at high p_T in 200 GeV data are very similar [28], one can show by using different scaling factors m_T spectra match at higher m_T. In this case, m_T spectra for baryons overshoot those for mesons at low m_T. The interpretation of m_T scaling is not settled yet, but from the experimental results presented here, it is clear that the spectral shape for mesons and baryons are very similar for both low and high m_T regions, but different for the intermediate m_T (1.5–2.5 GeV/c^2) region. In Section IV C, we will discuss the spectral shape at low m_T in detail, by taking into account the hadron mass effect.

TABLE III: Fitting results for A, T of Eq. 9 for p_T spectra for $\pi^\pm$, $K^\pm$, p, and $\overline{p}$ in 200 and 62.4 GeV $p + p$ collisions. The fitting range is fixed as $p_T = 0.5$–1.5 GeV/c for $\pi^\pm$, 0.6–2.0 GeV/c for $K^\pm$, and 0.8–2.5 GeV/c for p, $\overline{p}$ at both collision energies.

$\sqrt{s}$ (GeV)	hadron	A	T (GeV/c)	χ^2/NDF
200	π^+	80.1 ± 7.2	0.220 ± 0.004	11.5/8
	π^-	80.7 ± 7.5	0.220 ± 0.004	13.5/8
	K^+	6.45 ± 0.50	0.296 ± 0.005	29.4/12
	K^-	6.62 ± 0.51	0.293 ± 0.004	18.8/12
	p	3.24 ± 0.38	0.318 ± 0.006	3.3/15
	$\overline{p}$	2.83 ± 0.35	0.318 ± 0.006	2.8/15
62.4	π^+	78.0 ± 7.0	0.203 ± 0.003	9.0/8
	π^-	81.0 ± 6.2	0.200 ± 0.003	11.1/8
	K^+	6.17 ± 0.52	0.264 ± 0.004	15.6/12
	K^-	6.01 ± 0.49	0.254 ± 0.004	10.0/12
	p	4.61 ± 0.48	0.275 ± 0.005	2.8/15
	$\overline{p}$	2.95 ± 0.36	0.267 ± 0.005	2.9/15

TABLE IV: Normalization scaling factors for m_T spectra for Fig. 7. The scaling factors for the STAR experiment are determined from [31, 33] and those for the ISR results are determined from [25].

$\sqrt{s}$ (GeV)	Exp.	π^+	π^-	π^0	K^+	K^-	K_s^0	p	$\overline{p}$	Λ	$\overline{\Lambda}$
200	PHENIX	1.0	1.0	0.9	2.4	2.4	-	1.15	1.4	-	-
200	STAR	1.0	1.0	-	-	-	2.4	0.75	0.75	0.8	0.9
62.4	PHENIX	1.0	1.0	0.9	2.32	2.88	-	0.9	1.5	-	-
63	ISR	-	-	-	-	-	-	-	-	0.4	0.5

C. $m_T - m$ spectra

Figure 8 shows the $m_T - m$ spectra for $\pi^\pm$, $K^\pm$, p, and $\overline{p}$ in 200 and 62.4 GeV $p + p$ collisions, respectively. When analyzing these $m_T - m$ spectra of various identified hadrons, one discusses the spectral shape mainly in the low $m_T - m$ region. Each of these spectra is fitted with an exponential functional form:

$$\frac{1}{2\pi m_T}\frac{d^2\sigma}{dy\,dm_T} = A \exp\left(-\frac{m_T - m}{T_{\rm inv}}\right) \quad (10)$$

where A is a normalization factor and $T_{\rm inv}$ is called the inverse slope parameter. The fitting parameters and χ^2/NDF by using Eq. 10 for $\pi^\pm$, $K^\pm$, p, and $\overline{p}$ in 200 and 62.4 GeV $p + p$ collisions, are tabulated in Table III. The fitting range is fixed as $m_T - m = 0.3$–1.0 GeV/c^2 for all particle species at both collision energies. We obtain smaller χ^2/NDF for protons and antiprotons than those for pions and kaons, because of the larger systematic uncertainties for p and $\overline{p}$ at low p_T due to the uncertainties of weak decay feed-down corrections. As seen in Fig. 8
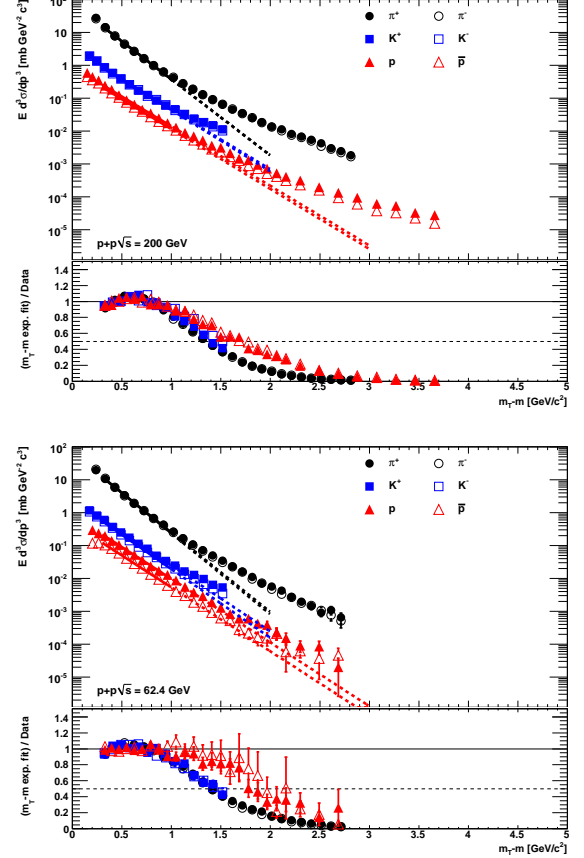

FIG. 8: (color online) $m_T - m$ spectra for $\pi^\pm$, $K^\pm$, p, and $\overline{p}$ in $p + p$ collisions at $\sqrt{s} =$ (upper) 200 and (lower) 62.4 GeV at midrapidity. Only statistical uncertainties are shown. Each spectrum is fitted with an exponential form of Eq. (10) in the range of $m_T - m = 0.3$–1.0 GeV/c^2. Solid lines represent the functions in the fitted range, dashed lines show the extrapolation of these functions beyond this range. (lower panels) Ratio of the exponential fit to data for each particle species.

the spectra are exponential in the low $m_T - m$ range. At higher transverse mass, the spectra become less steep, corresponding to an emerging power law behavior. The transition from exponential to power law can be seen at $m_T - m = 1$–2 GeV/c^2 for all particle species.

The dependence of $T_{\rm inv}$ on hadron mass is shown in Fig. 9. These slope parameters are almost independent of the energy of $\sqrt{s} = 62.4$ and 200 GeV. The inverse slope parameters of kaons is similar to that of protons while the slope parameter of pions has slightly smaller values. It may be possible that lower $T_{\rm inv}$ values for pions are due to pions from resonance decays (e.g. ρ, Λ), although such an effect is reduced by the lower transverse momentum cut. An alternative explanation is that hydrodynamical collective behavior may develop even in the small $p + p$ system, which we will explore at Section V A.

In Fig. 10, the collision energy dependence of $T_{\rm inv}$ is shown by compiling results from past experiments [24, 33, 48–50]. The values of $T_{\rm inv}$ reported here are obtained
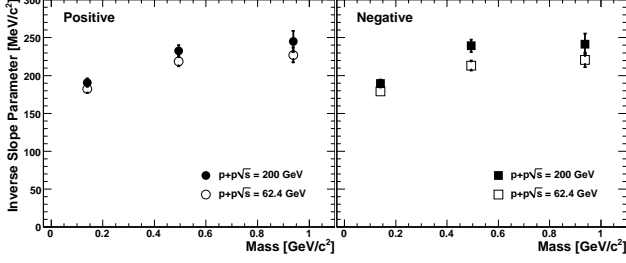
FIG. 9: Inverse slope parameter $T_{\rm inv}$ for $\pi^{\pm}$, $K^{\pm}$, p and $\overline{p}$ in $p + p$ collisions at $\sqrt{s}$ = 200 GeV and 62.4 GeV. The fitting range is $m_T - m$ = 0.3–1.0 GeV/c^2 for all particle species at both collision energies. The errors are statistical and systematic combined. The statistical errors are negligible.

TABLE V: Fitting results for A, $T_{\rm inv}$ of Eq. 10 for $\pi^{\pm}$, $K^{\pm}$, p, and $\overline{p}$ in 200 and 62.4 GeV $p + p$ collisions. The fitting range is fixed as $m_T - m$ = 0.3–1.0 GeV/c^2 for all particle species at both collision energies.

$\sqrt{s}$ (GeV)	hadron	A	$T_{\rm inv}$ (GeV/c^2)	χ^2/NDF
200	π^+	73.4 ± 7.1	0.190 ± 0.005	5.6/5
	π^-	74.8 ± 7.2	0.189 ± 0.005	3.1/5
	K^+	3.25 ± 0.29	0.232 ± 0.007	3.6/6
	K^-	2.99 ± 0.27	0.239 ± 0.008	3.6/6
	p	0.85 ± 0.14	0.245 ± 0.014	1.0/7
	$\overline{p}$	0.74 ± 0.13	0.241 ± 0.014	0.5/7
62.4	π^+	61.7 ± 5.9	0.182 ± 0.005	3.1/5
	π^-	65.2 ± 5.3	0.179 ± 0.004	4.7/5
	K^+	2.44 ± 0.22	0.219 ± 0.007	2.6/6
	K^-	2.21 ± 0.20	0.213 ± 0.006	4.6/6
	p	0.81 ± 0.10	0.227 ± 0.010	1.1/7
	$\overline{p}$	0.49 ± 0.07	0.221 ± 0.010	0.3/7

by fitting all the p_T spectra in the same way. The fitting range is $m_T - m$ = 0.3–1.0 GeV/c^2 for all particle species in all collision systems. The $T_{\rm inv}$ values for RHIC energies are consistent with earlier experimental results at other energies [24, 48–50]. For both pions and kaons, the inverse slope parameters increase with collision energy from $T_{\rm inv}$ = 120 MeV/c^2 to 170 MeV/c^2 (240 MeV/c^2) for pions (kaons) up to $\sqrt{s}$ = 200 GeV. According to Tevatron data, $T_{\rm inv}$ seems to be saturated at $\sqrt{s}$ above 200 GeV. The inverse slope parameters of protons and antiprotons indicate an increase at lower $\sqrt{s}$ which keeps on increasing even at Tevatron energies. We look forward to data from the LHC to further clarify these issues.

D. Particle ratios

Figures 11 and 12 show particle ratios such as antiparticle-to-particle, K/π, p/π as a function of p_T.

The π^-/π^+ and K^-/K^+ ratios show a flat p_T dependence at both 200 and 62.4 GeV energies. The π^-/π^+ ratio is almost unity at both energies. The K^-/K^+ ratio is consistent with unity at $\sqrt{s}$ = 200 GeV, while it decreases to 0.8–0.9 in the measured p_T range at 62.4 GeV. On the other hand, $\overline{p}/p$ ratio seems to be a decreasing function of p_T at 200 GeV, from the value of $\approx$ 0.8 at p_T = 1.0 GeV/c to 0.6 at p_T = 4.5 GeV/c. Note that we fit the $\overline{p}/p$ ratio for 200 GeV $p + p$ from p_T = 1–4.5 GeV/c to a linear function, $a + bp_T$, which gives a = 0.93 ± 0.02, b = -0.07 $\pm$ 0.01. This decrease, also seen at lower $\sqrt{s}$ [24], might be the result of a difference of fragmentation between quark jet and gluon jet at high p_T region as suggested by the DSS fragmentation functions [47]. However, the NLO pQCD calculation using the DSS fragmentation functions (lines on the panels for $\overline{p}/p$ ratios) shows this effect is in disagreement with the measured $\overline{p}/p$ ratios. At 62.4 GeV, we can not conclude on the significance of the decrease of the $\overline{p}/p$ ratios as a function of p_T due to large statistical fluctuations. It is important to note agreement of the ISR measurements of the anti-particle to particle ratios as a function of p_T at $\sqrt{s}$ = 62.4 GeV (Fig. 11) with the present measurements except for the $\overline{p}/p$ ratio where there is a large discrepancy. The $\overline{p}/p$ ratio integrated over all p_T decreases from 0.8 at 200 GeV to 0.5 at 62.4 GeV (see further discussion in Section IV E). At low p_T, the large systematic uncertainties of the $\overline{p}/p$ ratio are due to the uncertainties of the weak decay feed down corrections.

Figure 12 presents the ratios of K^+/π^+, K^-/π^-, p/π^+, p/π^0, $\overline{p}/\pi^-$, and $\overline{p}/\pi^0$ as a function of p_T. Both the K^+/π^+ and the K^-/π^- ratios increase with increasing p_T up to the p_T = 2 GeV/c limit of the measurement. Both the p/π^0 and the $\overline{p}/\pi^0$ ratios seem to increase with p_T for p_T > 2 GeV/c, although the $\overline{p}/\pi^0$ ratio is relatively flat at $\sqrt{s}$ = 200 GeV in the same transverse momentum region. Clearly, better statistics are required to reach a firm conclusion. As a function of $\sqrt{s}$ the K^+/π^+, $\overline{p}/\pi^-$ and $\overline{p}/\pi^0$ ratios do not change significantly, while the K^-/π^- ratio increases and the p/π^+ and p/π^0 ratios decrease significantly for p_T > 1 GeV/c as the collision energy is increased from $\sqrt{s}$ = 62.4 GeV to 200 GeV.

E. $\langle p_T \rangle$ and dN/dy

Mean transverse momentum $\langle p_T \rangle$ and particle yield per unit rapidity dN/dy are determined by integrating the measured p_T spectrum for each particle species. For the unmeasured p_T region, we fit the measured p_T spectrum with a Tsallis function [52] given below, as in a related publication [28], and also with an m_T exponential function, then extrapolate the obtained function to the unmeasured p_T region. The p_T ranges for fitting are: 0.4–3.0 GeV/c for pions, 0.4–2.0 GeV/c for kaons, 0.5–4.0 GeV/c for protons and antiprotons.

The final yield dN/dy is calculated by taking the sum of the yield from the data, and the yield from the func-
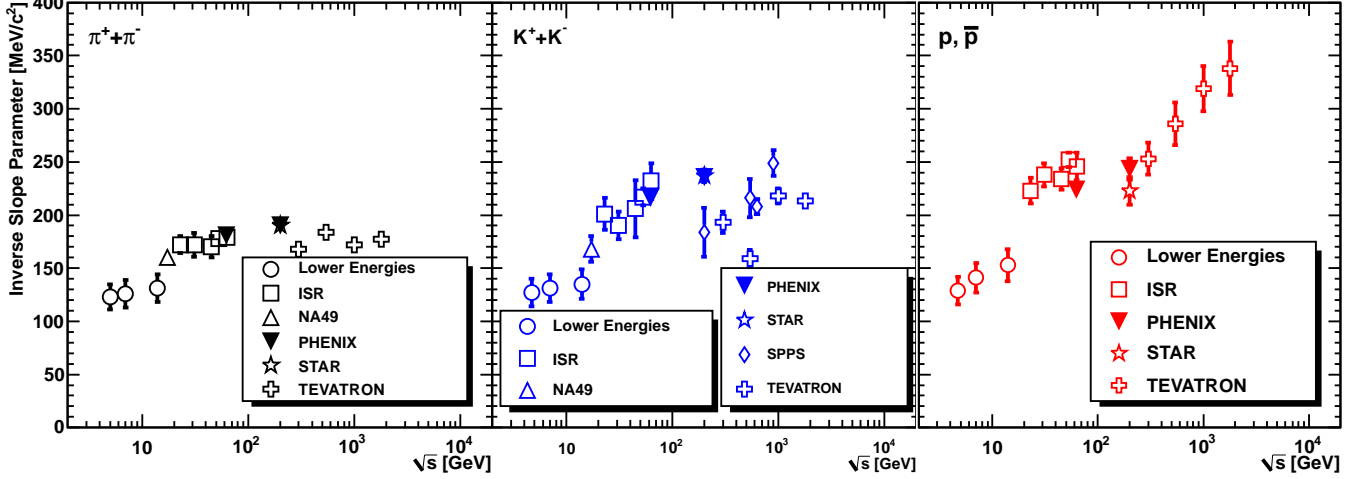
FIG. 10: (color online) Inverse slope parameter T_{inv} for $\pi^+ + \pi^-$, $K^+ + K^-$, p and $\overline{p}$ in $p + p$ and $p + \overline{p}$ collisions versus collision energy $\sqrt{s}$. The fitting range is $m_T - m = 0.3$–1.0 GeV/c^2 for all particle species for all collision systems. The errors are statistical and systematic combined. The statistical errors are negligible. The other experimental data are taken from [24, 33, 48–50].

TABLE VI: Fitting results from using the Tsallis distribution (Eq. 11) for $\pi^\pm$, $K^\pm$, p and $\overline{p}$ in $p + p$ collisions at $\sqrt{s} = 200$ and 62.4 GeV.

$\sqrt{s}$ (GeV)	hadron	dN/dy	q	C	χ^2/NDF
200	π^+	0.963 ± 0.071	8.24 ± 0.33	0.115 ± 0.006	4.3/23
	π^-	0.900 ± 0.063	8.95 ± 0.39	0.123 ± 0.006	3.2/23
	K^+	0.108 ± 0.006	6.25 ± 0.64	0.137 ± 0.011	1.6/13
	K^-	0.103 ± 0.005	7.00 ± 0.78	0.147 ± 0.011	2.9/13
	p	0.044 ± 0.004	11.1 ± 1.6	0.184 ± 0.014	4.1/22
	$\overline{p}$	0.037 ± 0.003	12.0 ± 1.8	0.186 ± 0.014	1.3/22
62.4	π^+	0.782 ± 0.056	12.1 ± 0.9	0.133 ± 0.007	4.6/22
	π^-	0.824 ± 0.053	11.9 ± 0.7	0.128 ± 0.006	4.8/22
	K^+	0.076 ± 0.003	10.2 ± 1.8	0.165 ± 0.012	4.9/13
	K^-	0.067 ± 0.003	11.6 ± 2.1	0.164 ± 0.011	2.2/13
	p	0.040 ± 0.003	24.5 ± 9.9	0.201 ± 0.015	7.1/21
	$\overline{p}$	0.022 ± 0.002	32.5 ± 21.0	0.202 ± 0.018	7.9/21

tional form in the unmeasured p_T region. The total inelastic cross sections are assumed to be 42.0 mb and 35.6 mb for 200 GeV and 62.4 GeV respectively. For $\langle p_T \rangle$, we integrate the measured p_T spectrum with p_T weighting, and then divide it by the obtained dN/dy. The final values are obtained by averaging the results of the two fits. The systematic uncertainties are evaluated as half of the difference between these fitting values.

- Tsallis distribution is given by Eq. 11 below. In this fitting form, the free parameters are dN/dy, q and C, while the mass m is fixed to the hadron mass. The fitting results are given in Table VI.

$$\frac{1}{2\pi p_T} \frac{d^2 N}{dy\,dp_T} =$$

$$\frac{dN}{dy} \frac{(q-1)(q-2)}{2\pi q C \left[qC + m(q-2) \right]} \left[1 + \frac{m_T - m}{qC} \right]^{-q} \quad (11)$$

- Exponential distribution in m_T is given by Eq. 12 below. The free fit parameters are the normalization constant A and the inverse slope parameter T_{inv}.

$$\frac{1}{2\pi p_T} \frac{d^2 N}{dy\,dp_T} = A \exp\left(-\frac{m_T}{T_{\text{inv}}} \right) \quad (12)$$

$$\frac{dN}{dy} = 2\pi A (m T_{\text{inv}} + T_{\text{inv}}^2) \quad (13)$$
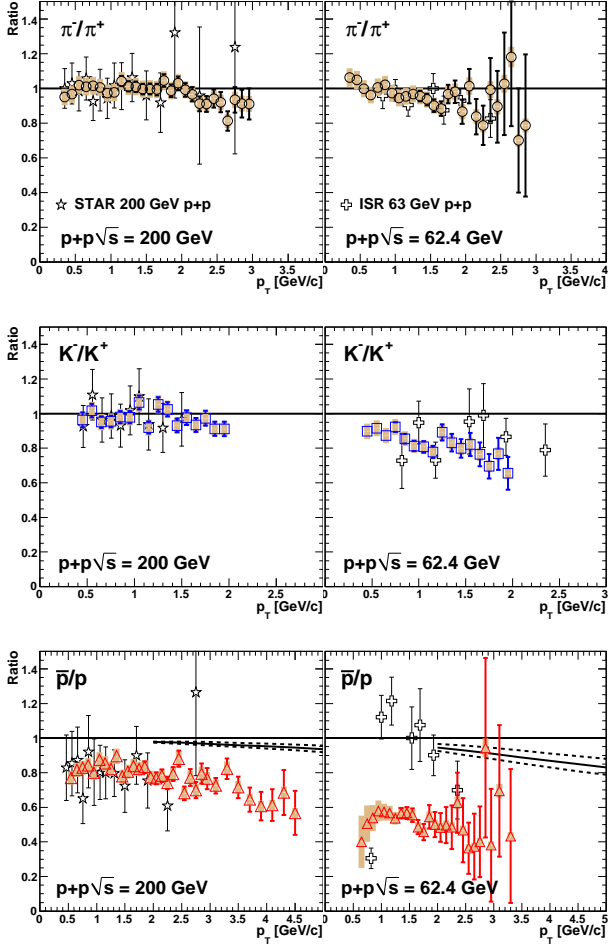
FIG. 11: (color online) π^-/π^+, K^-/K^+, $\overline{p}/p$ ratios as a function of p_T in $p+p$ collisions at $\sqrt{s}$ = (left) 200 and (right) 62.4 GeV. Systematic uncertainties are shown as vertical shaded band. STAR data are from [51] and ISR data are from [24]. For $\overline{p}/p$ ratios, the NLO pQCD calculations using the DSS fragmentation functions [47] are also shown as (solid lines) $\mu = p_T$ and (dashed lines) $\mu = 2p_T$, $p_T/2$.

The obtained $\langle p_T \rangle$ values are summarized in Table VII. They are plotted in Fig. 13, which indicates a clear increase of $\langle p_T \rangle$ with hadron mass. The values at 200 GeV are almost same as those for 62.4 GeV data. If the spectral shape is a pure exponential, $\langle p_T \rangle$ should be equal to $2T_{inv}$ analytically. By comparing Tables V and VII, the measured $\langle p_T \rangle$ is almost $2T_{inv}$ for pions. But for kaons and (anti)protons, the measured $\langle p_T \rangle$ is systematically larger than $2 T_{inv}$. This demonstrates that the spectral shape at low p_T is not a pure exponential especially for kaons and (anti)protons.

The collision energy dependence of $\langle p_T \rangle$ for each particle type is shown in Fig. 14. Data shown here are: lower energy data [48], ISR data [24], Tevatron data [49, 53], and RHIC data from STAR [33] and PHENIX (present study). The $\langle p_T \rangle$ values for all the other experiments have been determined by fitting the p_T spectra. For pi-
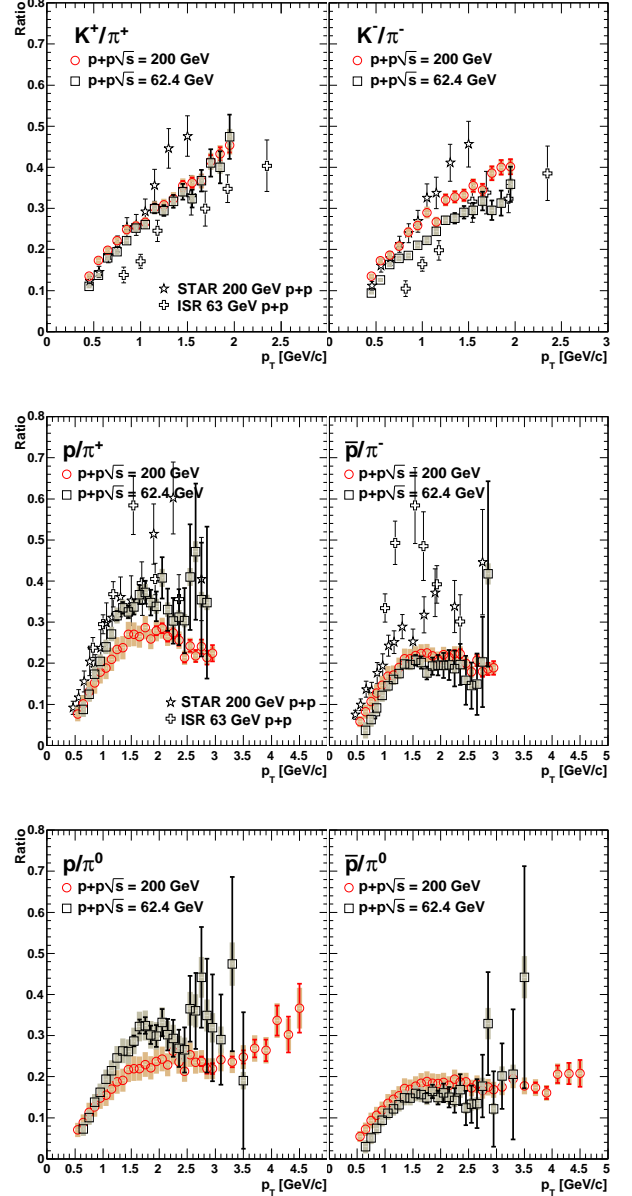
FIG. 12: (color online) (top) K^+/π^+ and K^-/π^- ratios, (middle) p/π^+ and (bottom) $\overline{p}/\pi^-$ ratios, and (bottom) p/π^0 and $\overline{p}/\pi^0$ ratios as a function of p_T in $p+p$ collisions at $\sqrt{s}$ = (left) 200 and (right) 62.4 GeV. Systematic uncertainties are shown as vertical shaded bands.

ons, the $\langle p_T \rangle$ shows a linear increase in $\ln(\sqrt{s})$. For kaons and (anti)protons the increase is much faster than those for pions. However, systematic issues at both lower and higher center-of-mass energies remain to be resolved.

Figure 15 shows the dependence of $\langle p_T \rangle$ on the centrality of the collisions (given by the number of participating nucleons, N_{part}) for $\pi^\pm$, $K^\pm$, p and $\overline{p}$ in Au+Au collisions at $\sqrt{s_{NN}}$ = 200 GeV [37] as compared to minimum bias $p + p$ collisions at $\sqrt{s}$ = 200 GeV (present analysis). The error bars in the figure represent the statistical errors.

The systematic errors from cut conditions are shown as shaded boxes on the right for each particle species. The systematic errors from extrapolations, which are scaled by a factor of two for clarity, are shown in the bottom for each particle species. It is found that $\langle p_T \rangle$ for all particle species increases from the most peripheral to midcentral collisions, and appears to saturate from the midcentral to central collisions. The $\langle p_T \rangle$ in $p+p$ are consistent with the expectation from the N_{part} dependence in Au+Au, and are similar to the values in peripheral Au+Au.
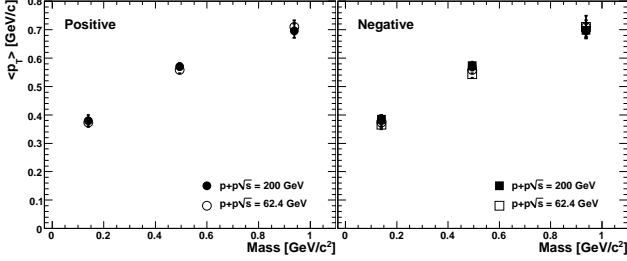
FIG. 13: Mean transverse momentum $\langle p_T \rangle$ as a function of mass in $p+p$ collisions at $\sqrt{s} = 200$ and 62.4 GeV. The errors are statistical and systematic combined. The statistical errors are negligible.

TABLE VII: Mean transverse momentum ($\langle p_T \rangle$) and particle yield (dN/dy) for $\pi^{\pm}$, $K^{\pm}$, p and $\overline{p}$ in $p+p$ collisions at $\sqrt{s} = 200$ and 62.4 GeV. The errors are statistical and systematic combined, but the statistical errors are negligible.

$\sqrt{s}$ (GeV)	hadron	$\langle p_T \rangle$ (GeV/c)	dN/dy
200	π^+	0.379 ± 0.021	0.842 ± 0.127
	π^-	0.385 ± 0.014	0.810 ± 0.096
	K^+	0.570 ± 0.012	0.099 ± 0.010
	K^-	0.573 ± 0.014	0.096 ± 0.009
	p	0.696 ± 0.025	0.043 ± 0.003
	$\overline{p}$	0.698 ± 0.023	0.035 ± 0.002
62.4	π^+	0.373 ± 0.013	0.722 ± 0.066
	π^-	0.366 ± 0.016	0.750 ± 0.079
	K^+	0.558 ± 0.012	0.072 ± 0.004
	K^-	0.544 ± 0.013	0.064 ± 0.004
	p	0.710 ± 0.023	0.034 ± 0.002
	$\overline{p}$	0.709 ± 0.040	0.018 ± 0.001

The dN/dy values at midrapidity are summarized in Table VII. They are plotted in Fig. 16 as a function of hadron mass for both 200 and 62.4 GeV collision energies. There are differences in the yield between 200 and 62.4 GeV especially for kaons and antiprotons continuing the trend observed at lower $\sqrt{s}$ [24]. It is interesting to note that even in the situation that dN/dy is different between $\sqrt{s} = 200$ and 62.4 GeV, $\langle p_T \rangle$ is quite similar for both energies.

Figure 17 shows dN/dy as a function of collision energy for each particle species. Our results on dN/dy are consistent with the those at ISR energies [24]. It should be noted that STAR quotes the nonsingle diffractive (NSD) multiplicity while our measurement quotes the inelastic multiplicity, normalizing the integrated measured inclusive cross section by the total inelastic cross section [54]. At $\sqrt{s} = 200$ GeV, the inelastic cross section (σ^{INEL}) is 42 mb [55], and the single diffractive (SD) cross section is almost equal to the double diffractive (DD) cross section, $\sigma_{NN}^{SD} \approx \sigma_{NN}^{DD} \approx 4$ mb [56]. As the single diffractive refers only to the projectile proton in a $p+p$ fixed target measurement, one has to subtract the SD cross section for each proton from the inelastic cross section to determine the NSD cross section [57]. The resulting NSD cross section (σ^{NSD}) should be $42 - 2 \times 4\mathrm{mb} = 34$ mb. The ratio of the NSD multiplicity to the inelastic multiplicity is: $\sigma^{INEL}/\sigma^{NSD} = 42/34 = 1.24$, i.e. the NSD multiplicity is 24% higher than the inelastic multiplicity, and this effect can be actually seen in the experimental data [58].

We would like to point out also that the NSD charged particle multiplicity at $\sqrt{s} = 200$ GeV by STAR is $\approx$ 20% larger than other NSD results [58]. By taking this fact and the difference between NSD and inelastic into account, one can naturally understand $\approx 50\%$ difference on yields between STAR and the present analysis, for pions and kaons, as shown in Fig. 17. For protons and antiprotons the difference between STAR and the present analysis is bigger than those in pions and kaons. In addition to the effects we have mentioned above, the weak decay feed-down correction can contribute to it, since we remove p and $\overline{p}$ from the weak decay (see Section III D), while STAR does not.

Figure 18 shows the collision centrality dependence of dN/dy per participant pair (0.5 N_{part}) in $p+p$ (present analysis) and Au+Au [37] collisions at $\sqrt{s_{NN}} = 200$ GeV. The error bars on each point represent the quadratic sum of the statistical errors and systematic errors from cut conditions. The statistical errors are negligible. The lines represent the effect of the systematic error on N_{part} which affects all curves in the same way. The data indicate that dN/dy per participant pair increases for all particle species with N_{part} up to ≈ 100, and saturates from the midcentral to the most central collisions. As seen in Fig. 15 for $\langle p_T \rangle$, the dN/dy values in $p+p$ are consistent with the expectation from the N_{part} dependence in Au+Au.

F. Nuclear Modification Factor R_{AA}

In order to quantify the modification effect in nucleus-nucleus (A+A) collisions with respect to nucleon-nucleon collisions, the nuclear modification factor R_{AA} is used. R_{AA} is the ratio between the yield in A+A scaled by the average number of binary nucleon-nucleon collisions ($\langle N_{\mathrm{coll}} \rangle$) and the yield in $p+p$, as defined by the following equation:
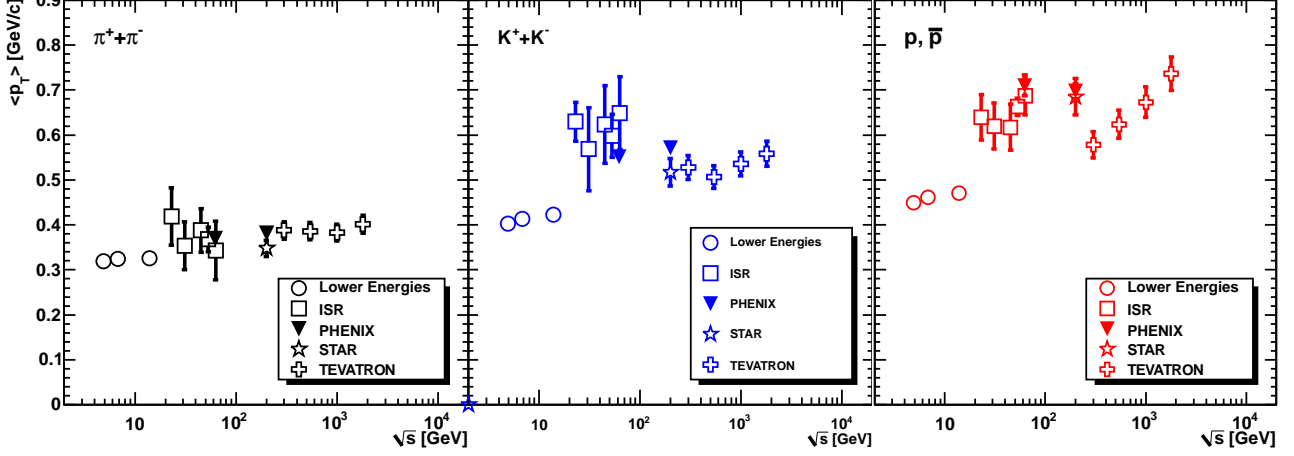
FIG. 14: (color online) Mean transverse momentum $\langle p_T \rangle$ for $\pi^+ + \pi^-$, $K^+ + K^-$, p and $\overline{p}$ as a function of $\sqrt{s}$ in $p + p$ and $p + \overline{p}$ collisions [24, 33, 48, 49, 53]. The errors are statistical and systematic combined. The statistical errors are negligible.
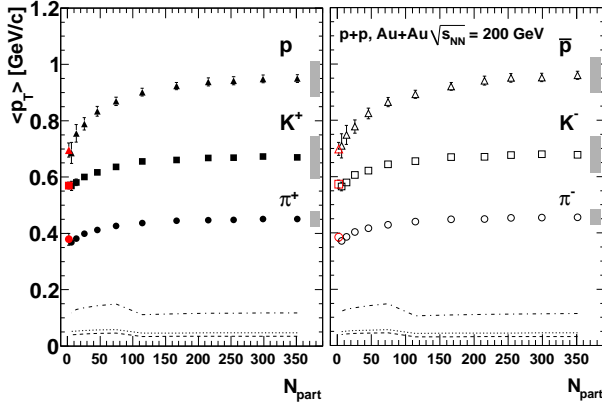

FIG. 15: (color online) Mean transverse momentum as a function of centrality (N_{part}) for pions, kaons, protons and anti-protons in in $p + p$ (present analysis, red color) and Au+Au [37] (black color) collisions at $\sqrt{s_{NN}} = 200$ GeV. The left (right) panel shows the $\langle p_T \rangle$ for positive (negative) particles. The error bars are statistical errors. The systematic errors from cuts conditions are shown as shaded boxes on the right for each particle species. The systematic errors from extrapolations, which are scaled by a factor of two for clarity, are shown in the bottom for protons and anti-protons (dashed-dot lines), kaons (dotted lines), and pions (dashed lines).

$$R_{\mathrm{AA}}(p_T) = \frac{(1/N_{\mathrm{AA}}^{\mathrm{evt}})\, \mathrm{d}^2 N_{\mathrm{AA}}/\mathrm{d}p_T dy}{\langle T_{\mathrm{AA}} \rangle \times \mathrm{d}^2 \sigma_{\mathrm{pp}}/\mathrm{d}p_T dy} \quad (14)$$

where $\langle T_{\mathrm{AA}} \rangle$ is the nuclear thickness function, defined as follows: $\langle T_{\mathrm{AA}} \rangle = \langle N_{\mathrm{coll}} \rangle / \sigma_{\mathrm{pp}}^{\mathrm{inel}}$. For the total A+A interaction cross section $\sigma_{\mathrm{AA}}^{\mathrm{int}}$ (minimum bias A+A collisions),
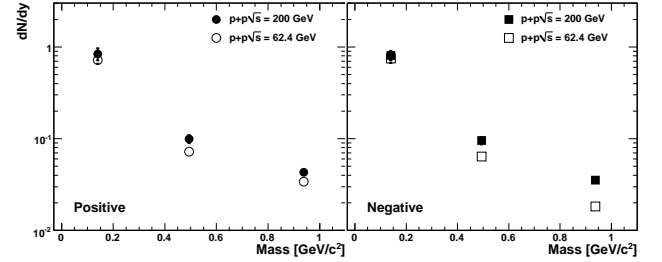
FIG. 16: Particle yield dN/dy as a function of mass in $p + p$ collisions at $\sqrt{s} = 200$ and 62.4 GeV. The errors are statistical and systematic combined. The statistical errors are negligible.

$\langle T_{\mathrm{AA}} \rangle = A^2/\sigma_{\mathrm{AA}}^{\mathrm{int}}$.

In general, R_{AA} is expressed as a function of p_T and collision centrality for A+A collisions. Due to the dominance of hard scatterings of partons at high p_T, R_{AA} is expected to be around unity above $p_T \approx 2$ GeV/c, if there is no yield modification by the nucleus in A+A. If there is a suppression (enhancement), R_{AA} is less than (greater than) unity. For the total A+A interaction cross section at a given p_T integrated over centrality (minimum bias A+A collisions) $\sigma_{\mathrm{AA}}(p_T) = A^2 \sigma_{\mathrm{pp}}(p_T)$ and $R_{\mathrm{AA}}(p_T) \equiv 1.0$.

Figure 19 shows the R_{AA} of $\pi^\pm$, π^0, $K^\pm$, p, and $\overline{p}$ in Au+Au collisions at $\sqrt{s_{NN}} = 200$ GeV at 0–5 % collision centrality. The data for identified charged hadrons in Au+Au at $\sqrt{s_{NN}} = 200$ GeV are taken from [37] measured by the PHENIX experiment, and those for $p+p$ are taken from the present analysis at $\sqrt{s} = 200$ GeV. The R_{AA} for neutral pions is taken from [59]. The overall normalization uncertainty on R_{AA} (13.8%) is shown as a shaded box around unity (at $p_T = 0.1$ GeV/c)), which is the quadratic sum of (1) the uncertainty of $p + p$ inelastic cross section (9.7%) and (2) the uncertainty $\langle N_{\mathrm{coll}} \rangle$
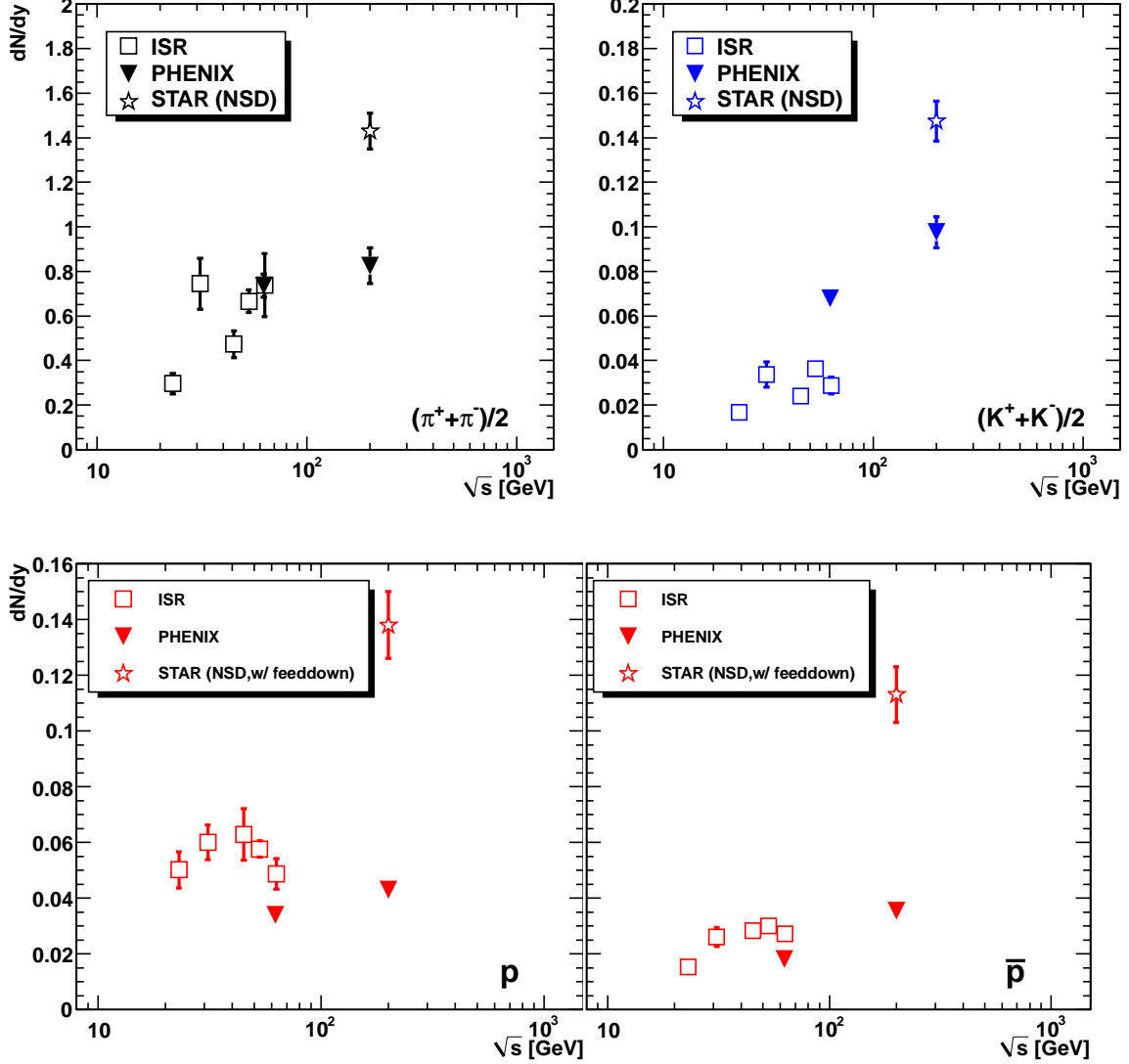
FIG. 17: (color online) (upper) Particle yield dN/dy at midrapidity for $(\pi^+ + \pi^-)/2$, $(K^+ + K^-)/2$ as a function of $\sqrt{s}$ in $p+p$ collisions [24, 29]. The errors are statistical and systematic combined, but the statistical errors are negligible. The dN/dy from STAR is determined for NSD $p+p$ events. (lower) Similar plots for p and $\overline{p}$ with feed-down correction applied to our data. The dN/dy from STAR is determined for NSD $p+p$ events, and is not corrected for weak-decay feed down.

(9.9%).

For pions R_{AA} is largely suppressed by a factor of ≈ 5, compared to $p+p$. This suppression effect is understood to be due to jet qu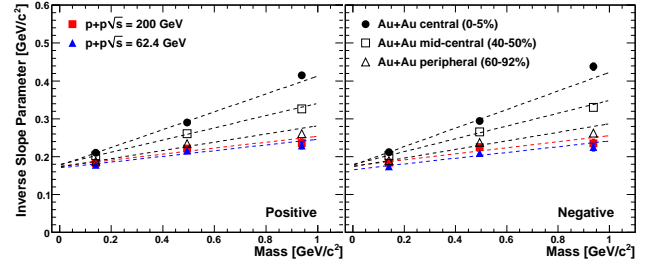enching or energy loss of partons in hot and dense medium created in Au+Au central collisions at RHIC energies [60, 61]. For kaons there is a similar trend as pions over a more limited p_T range. For protons and antiprotons there is an enhancement in $p_T = 2$–4 GeV/c. As reported in [26, 37, 62], possible explanations of the observed enhancements include the quark recombination model [63–65] and/or strong partonic and hadronic radial flow [66].

V. DISCUSSION

In this section, we discuss (1) soft particle production at low p_T, including the possibility of radial flow in $p+p$ collisions, and (2) the transition from soft to hard process, and hadron fragmentation at high p_T, where we show the x_T scaling of measured spectra, and make a comparison with NLO and NLL pQCD calculations.

A. Radial flow

In heavy ion collisions at RHIC energies, it is found that the inverse slope parameter (T_{inv}) of $m_T - m$ spectra
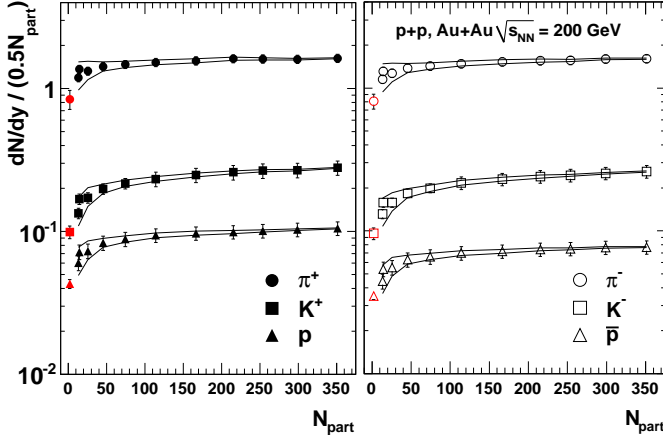
FIG. 18: (color online) Particle yield per unit rapidity (dN/dy) per participant pair $(0.5\ N_{\mathrm{part}})$ as a function of N_{part} for pions, kaons, protons and antiprotons in $p+p$ (present analysis, red color) and Au+Au collisions [37] at $\sqrt{s_{NN}} = 200$ GeV. The left (right) panel shows the dN/dy for positive (negative) particles. The error bars represent the quadratic sum of statistical errors and systematic errors from cut conditions. The lines represent the effect of the systematic error on N_{part} which affects all curves in the same way.

FIG. 19: (color online) R_{AA} of $\pi^{\pm}$, π^0, $K^{\pm}$, p, and $\overline{p}$ in Au+Au collisions at $\sqrt{s_{NN}}$ = 200 GeV at 0–5 % collision centrality. The data for identified charged hadrons in Au+Au at $\sqrt{s_{NN}} = 200$ GeV is taken from [37] and the data for $p+p$ is taken form the present analysis at $\sqrt{s} = 200$ GeV. The neutral pions (PHENIX) is taken from [59]. The statistical uncertainties are shown as bars, and the systematic uncertainties are shown as shaded boxes on each data point. The overall normalization uncertainty on R_{AA} (13.8%) is shown in the shaded box around unity (at $p_T = 0.1$ GeV/c)), which is the quadratic sum of (1) uncertainty of $p+p$ inelastic cross section (9.7%) and (2) uncertainty $\langle N_{\mathrm{coll}} \rangle$ (9.9%).

has a clear dependence on the hadron mass, i.e. heavier particles have larger inverse slope parameters [37, 67]. T_{inv} increases almost linearly as a function of particle mass; is largest when the nucleus-nucleus collision has a small impact parameter (central collisions); and is smallest for the collisions with a large impact parameter (peripheral collisions), as shown in Fig. 20.

This experimental observation can be interpreted as the existence of a radial flow generated by violent nucleon-nucleon collisions in two colliding nuclei and developed both in the quark-gluon plasma (QGP) phase and in hadronic rescatterings [66]. The radial flow velocity increases the transverse momentum of particles proportional to their mass, thus T_{inv} increases linearly as a function of particle mass. It is interesting to determine whether or not such an expansion is observed in high energy $p + p$ collisions [53].

Figure 20 shows the mass dependence of inverse slope parameter T_{inv} in $m_T - m$ spectra for positive (left) and negative (right) particles in $p + p$ collisions at $\sqrt{s} = 200$ and 62.4 GeV (also shown in Fig. 9), as well as for peripheral, midcentral and central in Au+Au collisions at $\sqrt{s_{NN}} = 200$ GeV [37]. The fit ranges are $m_T - m = 0.2$–1.0 GeV/c^2 for pions, and $m_T - m = 0.1$–1.0 GeV/c^2 for kaons, protons, and antiprotons, which are chosen in order to perform a fair comparison with T_{inv} in Au+Au collisions at RHIC [37]. The values of T_{inv} in $p + p$ for these fit ranges (see Table VIII) are all lower by roughly one standard deviation from the values in Table V for the common fit range of $m_T - m = 0.3$–1.0 GeV/c^2.

FIG. 20: (color online) Mass dependence of inverse slope parameter T_{inv} in $m_T - m$ spectra for (left) positive and (right) negative hadrons in $p+p$ collisions at $\sqrt{s} = 200$ and 62.4 GeV, as well as for peripheral, midcentral and central in Au+Au collisions at $\sqrt{s_{NN}} = 200$ GeV [37]. The errors are statistical and systematic combined, smaller than symbols. The statistical errors are negligible. The fit ranges are 0.2–1.0 GeV/c^2 for pions and 0.1–1.0 GeV/c^2 for kaons, protons, and antiprotons in $m_T - m$ [37]. The dotted lines represent a linear fit of the results for each data set, as a function of mass using Eq. (15).

In general, the inverse slope parameters increase with increasing particle mass in both Au+Au and $p + p$ collisions at 200 GeV. However, this increase is only modest in $p+p$ collisions and slightly weaker than in 60–92% central Au+Au collisions at 200 GeV. Also note that there is a mean multiplicity dependence of the transverse momentum spectra in $p + p$ collisions [49], that is not discussed in the present paper.

TABLE VIII: Inverse slope parameter T_{inv} for $\pi^{\pm}$, $K^{\pm}$, p and $\overline{p}$ for $p + p$ collisions at $\sqrt{s} = 200$ and 62.4 GeV. The fit ranges are 0.2–1.0 GeV/c^2 for pions and 0.1–1.0 GeV/c^2 for kaons, protons, and antiprotons in $m_T - m$. These fit ranges are chosen in order to perform a comparison with T_{inv} in Au+Au collisions at RHIC [37]. The errors are statistical and systematic combined, but the statistical errors are negligible.

$\sqrt{s}$ (GeV)	hadron	T_{inv} (MeV/c^2)	χ^2/NDF
200	π^+	183 ± 4	12.9/6
	π^-	184 ± 4	7.5/6
	K^+	221 ± 5	10.0/8
	K^-	225 ± 6	12.4/8
	p	236 ± 10	2.3/10
	$\overline{p}$	235 ± 10	1.2/10
62.4	π^+	178 ± 4	5.7/6
	π^-	174 ± 3	9.8/6
	K^+	216 ± 5	3.0/8
	K^-	209 ± 5	5.3/8
	p	230 ± 8	1.4/9
	$\overline{p}$	225 ± 9	2.0/9

TABLE IX: The extracted fit parameters of the freeze-out temperature (T_0) and the measure of the strength of the average radial transverse flow ($\langle u_t \rangle$) using Eq. (15). The fit results shown here are for positive and negative particles, and for the two different energies.

$\sqrt{s}$ (GeV)	$\pm$	T_0 (MeV/c^2)	$\langle u_t \rangle$	χ^2/NDF
200	Positive	175 ± 5	0.28 ± 0.02	4.1/1
	Negative	176 ± 5	0.28 ± 0.02	6.0/1
62.4	Positive	170 ± 5	0.27 ± 0.02	5.4/1
	Negative	165 ± 4	0.28 ± 0.02	3.8/1

We use a radial flow picture [68, 69] with the fitting function:

$$T = T_0 + m\langle u_t \rangle^2, \qquad (15)$$

where T_0 is a hadron freeze-out temperature and $\langle u_t \rangle$ is a "measure" of the strength of the (average radial) transverse flow. The relationship between the averaged transverse velocity ($\langle \beta_t \rangle$) and $\langle u_t \rangle$ is given by

$$\langle \beta_t \rangle = \langle u_t \rangle / \sqrt{1 + \langle u_t \rangle^2}. \qquad (16)$$

The dotted lines in Fig. 20 represent the linear fit to the $p + p$ collisions at $\sqrt{s} = 200$ and 62.4 GeV, that are compared to those in Au+Au collisions at $\sqrt{s_{NN}} = 200$ GeV in three different collision centrality classes. The fit results in $p + p$ are also given in Table IX. For Au+Au most central data (0–5%), $\langle u_t \rangle \approx 0.49 \pm 0.07$, while in $p + p$, $\langle u_t \rangle \approx 0.28$ at both 62.4 GeV and 200 GeV. While

this radial flow model is consistent with the data in central and midcentral Au+Au, i.e. $\pi/K/p$ points are on a straight line, it does not give a good description of either peripheral Au+Au or $p + p$ collisions (poor χ^2 in Table IX). This can be interpreted that radial flow is absent in $p + p$, where the $\pi/K/p$ points are obviously not on a straight line (Fig. 9), and that the radial flow develops only for a larger system.

B. x_T scaling

From the measurements of p_T spectra of hadrons in $p + p$ collisions, it is known that fragmentation of hard scattered partons is the dominant production mechanism of high p_T hadrons. It has been predicted theoretically from general principles, that such a production mechanism leads to a data scaling behavior called "x_T scaling" [36], where the scaling variable is defined as $x_T = 2p_T/\sqrt{s}$. Such a data scaling behavior was seen first on preliminary ISR data at CERN as reported in [36].

In the kinematic range corresponding to the x_T scaling limit, the invariant cross section near midrapidity can be written as:

$$E\frac{d^3\sigma}{dp^3} = \frac{1}{p_T{}^{n_{\text{eff}}}}F(x_T) = \frac{1}{\sqrt{s}^{n_{\text{eff}}}}G(x_T), \qquad (17)$$

where $F(x_T)$ and $G(x_T)$ are universal scaling functions. The parameter n_{eff} is characteristic for the type of interaction between constituent partons. For example for single photon or vector gluon exchange, $n_{\text{eff}} = 4$ [1]. Because of higher order effects, the running of the strong coupling constant $\alpha_s = \alpha_s(Q^2)$, the evolution of the parton distribution functions and fragmentation functions, and nonvanishing transverse momentum k_T of the initial-state, n_{eff} in general is not a constant but a function of x_T and $\sqrt{s}$, i.e. $n_{\text{eff}} = n_{\text{eff}}(x_T, \sqrt{s})$. This n_{eff} corresponds to the logarithmic variation of yield ratios at the same x_T for different $\sqrt{s}$ [70]. Note that the x_T scaling power n_{eff} is different from the exponent n that characterizes the power-law behavior of the single particle invariant spectrum at high p_T.

The value of n_{eff} depends on both the value of $\sqrt{s}$ and the range of x_T and depending on the reaction tends to settle at an asymptotic value between 6 and 4.5 where hard-scattering dominates and higher twist effects are small. This fact can also be used to determine the transition between soft and hard particle production mechanisms.

Earlier measurements of $n_{\text{eff}}(x_T, \sqrt{s})$ in $p+p$ collisions found values in the range of 5–8 [35, 36, 71–74]. Here we present the PHENIX results for the x_T scaling of pions, protons, and antiprotons and compare them with earlier data measured at various different values of $\sqrt{s}$. Due to the limited p_T range of our kaon measurements, kaons are not included in these comparisons.

We have evaluated the x_T-scaling power n_{eff} using two different methods that are both based on Eq. (17):
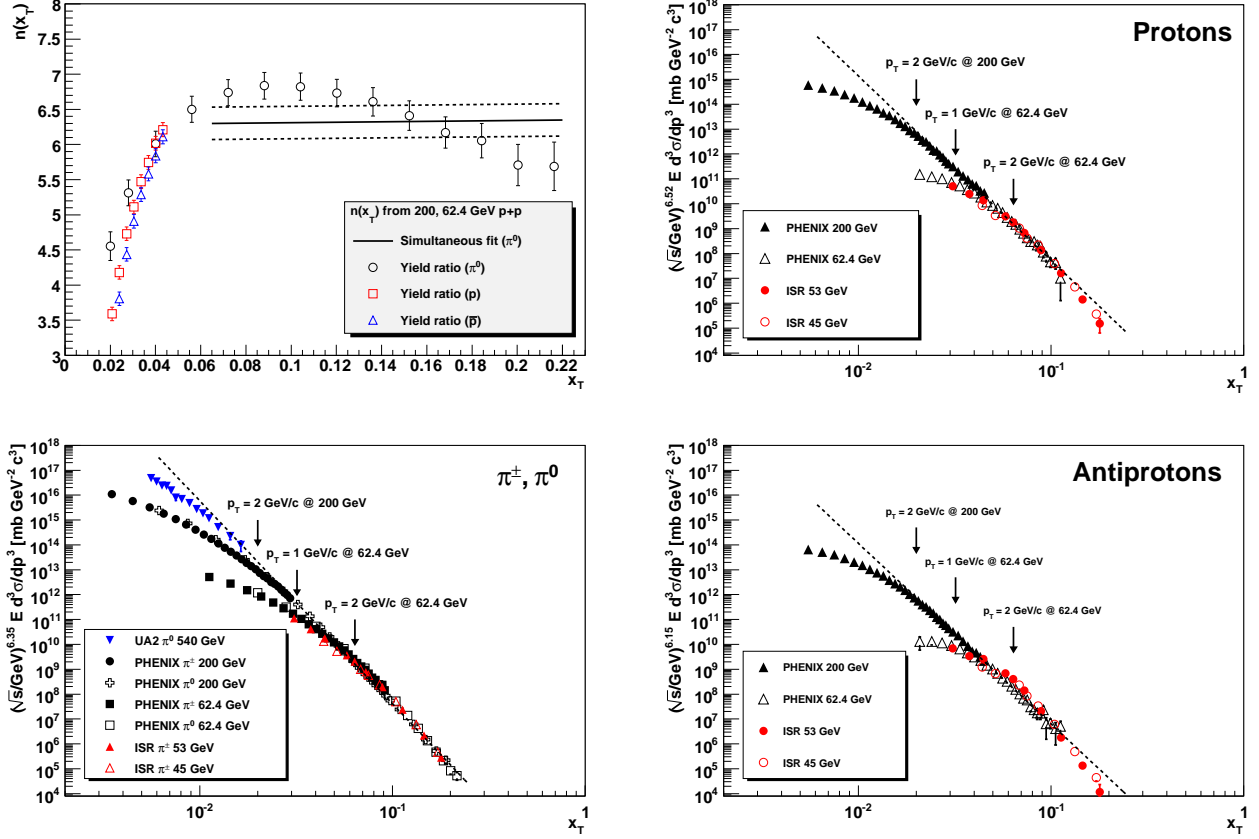
FIG. 21: (color online) (upper left) x_T-scaling power n_{eff} as determined from the ratios of yields as a function of x_T, for (open circle) neutral pions, (open square) protons, and (open triangle) antiprotons using $p + p$ data at $\sqrt{s} = 200$ and 62.4 GeV energies. The error of each data point is from the systematic and statistical errors of p_T spectra. The other plots show x_T spectra for (lower left) pions ($\pi^\pm$, π^0), (upper right) protons, and (lower right) antiprotons in $p + p$ collisions at different $\sqrt{s}$ at midrapidity. Only statistical uncertainties are shown. The dashed curves are the fitting results.

Method 1 is based on the linear variation of the logarithm of the ratio of the yields at different $\sqrt{s}$:

$$n_{eff}(x_T) = \frac{\log(Yield(x_T, 62.4)/Yield(x_T, 200))}{\log(200/62.4)}. \quad (18)$$

The $n_{\text{eff}}(x_T)$ is shown in Fig. 21 as a function of x_T for neutral pions, protons, and antiprotons for $p + p$ collisions at RHIC.

Method 2 is based on fitting the x_T distributions for a given type of particle measured at different energies. A common fitting function is defined as follows:

$$E\frac{d^3\sigma}{dp^3} = \left(\frac{A}{\sqrt{s}}\right)^{n_{\text{eff}}} x_T^{-m}, \quad (19)$$

limiting the fitting region to the high transverse momentum region ($p_T > 2$ GeV/c).

The x_T distributions for pions, protons, and antiprotons are shown in Fig. 21. PHENIX data are presented together with earlier data of [24, 30, 34, 75]. Dashed curves show the fitting results. The obtained n_{eff} values are summarized in Table X.

The exponent n_{eff} of the x_T scaling is found to have similar values for different particles, in the range of 6.3–6.5 for pions, protons, and antiprotons. The data points deviate from the x_T scaling in the transverse momentum region of $p_T < 2$ GeV/c. This scaling violation may be interpreted as a transition from hard to soft multiparticle production. For the highest x_T points for protons and antiprotons (but not for pions) the asymptotic x_T curve gets steeper. Further measurements at larger x_T, possibly at lower center-of-mass energies are needed to clarify this point.

C. Comparison to NLO and NLL pQCD calculations

In Figs. 22 to 23, our results for pion, proton and antiproton p_T spectra at $\sqrt{s} = 200$ and 62.4 GeV in $p + p$ collisions are compared to the NLO pQCD calculations.
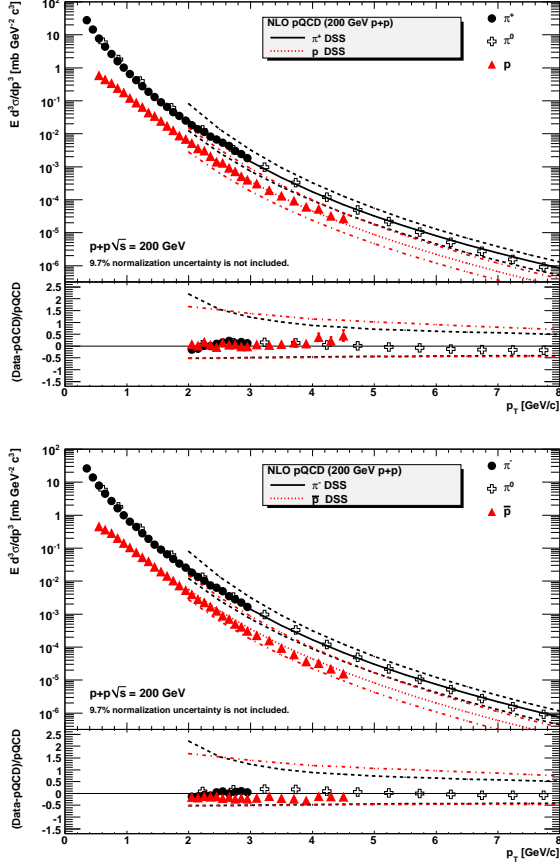
FIG. 22: (color online) Transverse momentum distributions for (upper) positive and (lower) negative particles at $\sqrt{s} = 200$ GeV in $p+p$ collisions. Only statistical uncertainties are shown. The normalization uncertainty (9.7%) is not included. NLO pQCD calculations (FF: DSS) are also shown. Solid lines are for $\mu = p_T$, and dashed lines are for $\mu = p_T/2, 2p_T$. The lower panel in each plot shows the ratio of (data - pQCD result)/pQCD result for each particle species.

TABLE X: Summary of x_T-scaling power $n_{\rm eff}$ in $p + p$ collisions. The errors are systematic error from the fitting.

hadron	A	$n_{\rm eff}$	m	χ^2/NDF
π	0.82 ± 0.08	6.35 ± 0.23	8.16 ± 0.22	156/31
p	1.12 ± 0.17	6.52 ± 0.59	7.41 ± 0.29	40/38
$\overline{p}$	0.84 ± 0.04	6.15 ± 0.05	7.26 ± 0.07	30/38

Because of the limited p_T reach in the measurements, the results for charged kaons are not compared to the NLO pQCD calculations. In these NLO pQCD calculations for $\eta < 1$ from W. Vogelsang [47] the cross section is factorized into initial parton distribution functions (PDFs) in the colliding protons, short-distance partonic hard-scattering cross sections which can be evaluated using perturbative QCD, and parton-to-hadron fragmentation functions (FFs).

For the description of the initial parton distributions, the Coordinated Theoretical-Experimental Project on QCD (CTEQ6M5) [76] PDFs are used. Different scales $\mu = p_T/2, p_T, 2p_T$ are utilized, where μ represents equal factorization, renormalization, and fragmentation scales. These provide initial conditions for the pQCD cross section calculations. Partons are then fragmented to hadrons with the help of the de Florian-Sassot-Stratmann (DSS) set of fragmentation functions which have the charge separation [77]. There are several other FFs, such as the "Albino-Kniehl-Kramer" (AKK) set of FFs [78], and the "Kniehl-Kramer-Potter" (KKP) set of FF [79]. Only the results for DSS FFs are shown in this paper, because they give better agreement with our measurements than other FFs. For example, in $p + p$ collisions at $\sqrt{s} = 200$ GeV the yields for $(p + \overline{p})/2$ in AKK (KKP) FFs are a factor of two smaller (larger) than the present measurement.

It is known that pion production in $\sqrt{s} = 200$ GeV $p+p$ collisions is reasonably well described by pQCD down to $p_T \sim 2$ GeV/c and up to $p_T \sim 20$ GeV/c [30, 33]. On the other hand, there are large variations in the p and $\overline{p}$ yields among various fragmentation functions [33] as we mentioned above. From the comparisons between baryon data and pQCD calculations at both $\sqrt{s} = 200$ and 62.4 GeV, it is potentially interesting to obtain a constraint on the fragmentation function, particularly the gluon fragmentation function for p and $\overline{p}$.

For the DSS fragmentation function, there is good agreement between the data and NLO pQCD calculations for pions and protons at 200 GeV, but not so good agreement with $\overline{p}$. It is more clearly shown in Fig. 11 that the $\overline{p}/p$ ratio at 200 GeV is not correctly described with NLO + DSS framework, which indicates that there is still room to improve the DSS fragmentation functions. The left-side plots of Fig. 23 show that for 62.4 GeV NLO + DSS pQCD calculations underestimate yields by a factor of two or three for all species. However, as it is still on the edge of the scale uncertainty of the NLO calculation, NLO pQCD agrees with the data within the large uncertainties.

As shown in [34], the NLL calculations give much better agreement with the data for π^0 in $p + p$ collisions at $\sqrt{s} = 62.4$ GeV. This means the resummed calculation is necessary to describe the cross section at 62.4 GeV. On the other hand, the resummation for $\sqrt{s} = 200$ GeV is not reliable, since the resummation can be done for a larger $x_T = 2p_T/\sqrt{s}$, which is not accessible for $\sqrt{s} = 200$ GeV data due to the p_T limitation. The right-side plots of Fig. 23 show the p_T distributions for $\pi^\pm$, p, and $\overline{p}$ in $p + p$ collisions at 62.4 GeV, together with the results of NLL pQCD calculations. The DSS FFs are used. It is found that the agreement between NLL pQCD and data is better than those for NLO pQCD.

The presented p_T spectra extend to the semi-hard 3–4 GeV/c region for pions and (anti)protons, which make them useful as a baseline to study in further detail the nuclear modification factor in A+A collisions. More de-
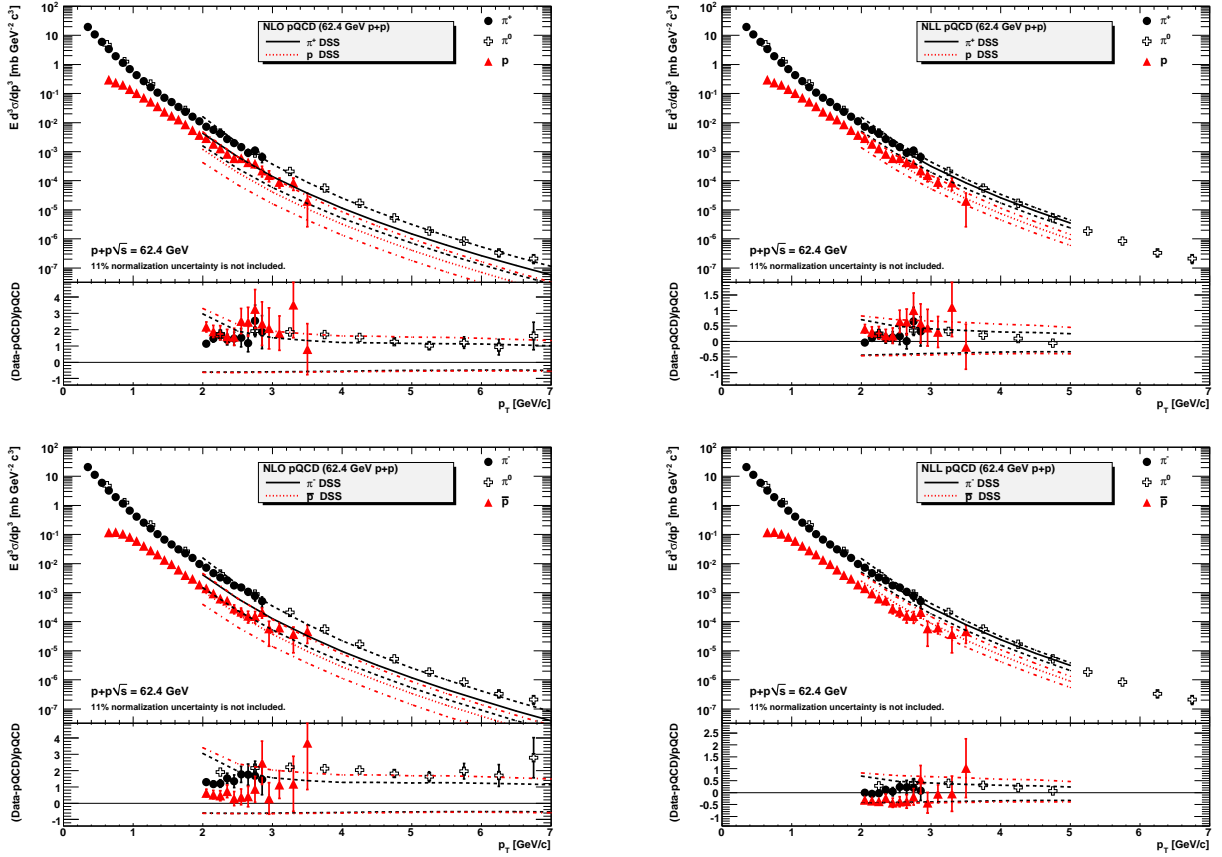
FIG. 23: (color online) Transverse momentum distributions for (upper) positive and (lower) negative particles at $\sqrt{s} = 62.4$ GeV in $p + p$ collisions. Only statistical uncertainties are shown. The normalization uncertainty (11%) is not included. (left) NLO and (right) NLL pQCD calculations (FF: DSS) are also shown. Solid lines are for $\mu = p_T$, and dashed lines are for $\mu = p_T/2, 2p_T$. The lower panel in each plot shows the ratio of (data - pQCD result)/pQCD result for each particle species.

tailed measurements at larger p_T are necessary for the further understanding of FFs and its particle species dependence at each beam energy.

VI. SUMMARY AND CONCLUSION

We presented transverse momentum distributions and yields for $\pi^{\pm}$, $K^{\pm}$, p and $\overline{p}$ in $p + p$ collisions at $\sqrt{s} = 200$ and 62.4 GeV at midrapidity, which provide an important baseline for heavy-ion-collision measurements at RHIC. The inverse slope parameter T_{inv}, mean transverse momentum $\langle p_T \rangle$, and yield per unit rapidity dN/dy are compared to the measurements at different $\sqrt{s}$ in $p + p$ and $p + \overline{p}$ collisions. While T_{inv} and $\langle p_T \rangle$ show a similar value for all particle species between 200 and 62.4 GeV, dN/dy shows a relatively large difference, especially for kaons and antiprotons, between 200 and 62.4 GeV. The $\overline{p}/p$ ratio is ~0.8 at 200 GeV, and ~0.5 at 62.4 GeV and the p_T dependence of the p/π^{+} (p/π^0) ratios varies between 62.4 and 200 GeV. Together with the measured dN/dy this gives insight on baryon transport and production at midrapidity.

We also analyzed the scaling properties of identified particle spectra, such as the m_T scaling and x_T scaling. Baryons and mesons are split in the m_T spectral shape at both 200 and 62.4 GeV. This splitting can be understood as the difference of hard production yields between baryons and mesons. The x_T scaling power n_{eff} shows similar values for pions, protons, and antiprotons.

We also compared the results in $p + p$ collisions at 200 GeV with the those in Au+Au at 200 GeV in the same experiment. It is found that T_{inv}, $\langle p_T \rangle$, and dN/dy change smoothly from $p + p$ to Au+Au, and all the values in $p + p$ are consistent with expectations from the N_{part} dependence in Au+Au. On the nuclear modification factor R_{AA}, there is a large suppression for pions, while there is an enhancement for protons and antiprotons at p_T =2–4 GeV/c. The observed suppression can be understood by the energy loss of partons in hot and dense medium created in Au+Au central collisions at RHIC energies [60, 61]. Possible explanations of the observed enhancements for protons and antiprotons include quark recombination [63–65] and/or strong partonic and hadronic radial flow [66].

Identified particle spectra are extended to the semi-

hard 3–4 GeV/c region for pions and (anti)protons, which make it possible to study in further detail the nuclear modification factor of identified particles in A+A collisions. NLO pQCD calculations with DSS fragmentation function show good agreement for pions and protons at 200 GeV while there is less good agreement with $\overline{p}$. This indicates that fragmentation functions can be improved further.

For 62.4 GeV, NLO pQCD calculations underestimate by a factor of two or three the yields for all particle species. On the other hand, NLL pQCD calculation gives a better agreement with the data. This suggests that resummed calculations are necessary to describe the cross section at 62.4 GeV.

From comparisons to some calculations such as NLO/NLL pQCD framework, one can discuss the mechanism of soft and hard particle production in $p + p$ collisions. There is a transition between these two regions ("soft-hard transition") at $p_T \sim 2$ GeV/c for pions, and at $p_T \sim 3$ GeV/c for (anti)protons, or equivalently, $m_T - m$ = 1–2 GeV/c^2 for all particle species at both energies. The fractions of soft and hard components gradually change in the transition region. The new measurements presented in this work indicate that the behavior of T_{inv} and $\langle p_T \rangle$ of identified particles in $p + p$ collisions needs improved systematics of measurement at both higher and lower $\sqrt{s}$ to clarify the precise $\sqrt{s}$ dependences.

Acknowledgments

[1] S. M. Berman, J. D. Bjorken, and J. B. Kogut, Phys. Rev. D **4**, 3388 (1971).

[2] J. Nishimura, Soryushiron Kenkyu **12**, 24 (1956).

[3] G. Cocconi, Phys. Rev. **111**, 1699 (1958).

[4] G. Cocconi, L. J. Koester, and D. H. Perkins, LRL Report **No. UCRL-10022**, 167 (1961), unpublished.

[5] J. Orear, Phys. Rev. Lett. **12**, 112 (1964).

[6] R. Hagedorn, pp. 13–46 (1995), invited talk at NATO Advanced Study Workshop on Hot Hadronic Matter: Theory and Experiment, Divonne-les-Bains, France, 27 Jun - 1 Jul 1994.

[7] J. Erwin, W. Ko, R. L. Lander, D. E. Pellett, and P. M. Yager, Phys. Rev. Lett. **27**, 1534 (1971).

[8] R. Hagedorn, Nucl. Phys. **B24**, 93 (1970).

[9] S. Barshay and Y. A. Chao, Phys. Lett. **B38**, 229 (1972).

[10] H. Bøggild et al. (Scandinavian Bubble Chamber Collaboration), Nucl. Phys. **B57**, 77 (1973).

[11] M. Deutschmann et al., Nucl. Phys. **B70**, 189 (1974).

[12] J. Bartke et al. (Aachen-Berlin-Bonn-CERN-Cracow-Heidelberg-Warsaw Collaboration), Nucl. Phys. **B120**, 14 (1977).

[13] B. Alper et al. (British-Scandinavian Collaboration), Nucl. Phys. **B100**, 237 (1975).

[14] M. Gell-Mann, Phys. Lett. **8**, 214 (1964).

[15] G. Zweig, CERN Reports **No. 8182/TH.401 and No. 8419/TH.412** (1964), unpublished.

[16] V. V. Anisovich and M. N. Kobrinsky, Phys. Lett. **B52**, 217 (1974), and references therein.

[17] R. P. Feynman, Phys. Rev. Lett. **23**, 1415 (1969).

[18] J. Benecke, T. T. Chou, C.-N. Yang, and E. Yen, Phys. Rev. **188**, 2159 (1969).

[19] A. H. Mueller, Phys. Rev. D **2**, 2963 (1970).

[20] U. Camerini, W. O. Lock, and D. H. Perkins, Progress in Cosmic Ray Physics **Volume I**, 1 (1952), ed. J.G. Wilson.

[21] W. B. Fowler, R. P. Shutt, A. M. Thorndike, and W. L. Whittemore, Phys. Rev. **95**, 1026 (1954).

[22] E. Fermi, Phys. Rev. **81**, 683 (1951).

[23] S. Z. Belenkij and L. D. Landau, Nuovo Cim. Suppl. **3S10**, 15 (1956), Usp. Fiz. Nauk **56**, 309 (1955).

[24] B. Alper et al. (British-Scandinavian Collaboration), Nucl. Phys. **B87**, 19 (1975).

[25] D. Drijard et al. (CERN-Dortmund-Heidelberg-Warsaw Collaboration), Zeit. Phys. **C12**, 217 (1982).

[26] S. S. Adler et al. (PHENIX Collaboration), Phys. Rev. C **74**, 024904 (2006), nucl-ex/0603010.

[27] S. S. Adler et al. (PHENIX Collaboration), Phys. Rev. Lett. **91**, 241803 (2003), hep-ex/0304038.

[28] K. Adcox et al. (PHENIX Collaboration), PPG **099**, (2010), -.

[29] B. I. Abelev et al. (STAR Collaboration) (2008), 0808.2041.

[30] A. Adare et al. (PHENIX Collaboration), Phys. Rev. D **76**, 051106 (2007), 0704.3599.

[31] B. I. Abelev et al. (STAR Collaboration), Phys. Rev. C **75**, 064901 (2007), nucl-ex/0607033.

[32] J. Adams et al. (STAR Collaboration), Phys. Rev. D **74**, 032006 (2006), nucl-ex/0606028.

[33] J. Adams et al. (STAR Collaboration), Phys. Lett. **B637**, 161 (2006), nucl-ex/0601033.

[34] A. Adare et al. (PHENIX Collaboration), Phys. Rev. D **79**, 012003 (2009), 0810.0701.

[35] P. Darriulat, Ann. Rev. Nucl. Part. Sci. **30**, 159 (1980).

[36] R. Blankenbecler, S. Brodsky, and J. Gunion, Phys. Lett. **B 42**, 461 (1972).

[37] S. S. Adler et al. (PHENIX Collaboration), Phys. Rev. C **69**, 034909 (2004), nucl-ex/0307022.

[38] K. Adcox et al. (PHENIX Collaboration), Nucl. Instrum. Meth. **A499**, 469 (2003).

[39] S. H. Aronson et al. (PHENIX Collaboration), Nucl. Instrum. Meth. **A499**, 480 (2003).

[40] M. Aizawa et al. (PHENIX Collaboration), Nucl. Instrum. Meth. **A499**, 508 (2003).

[41] M. Allen et al. (PHENIX Collaboration), Nucl. Instrum. Meth. **A499**, 549 (2003).

[42] K. Adcox et al. (PHENIX Collaboration), Nucl. Instrum. Meth. **A499**, 489 (2003).

[43] J. T. Mitchell et al. (PHENIX Collaboration), Nucl. Instrum. Meth. **A482**, 491 (2002), nucl-ex/0201013.

[44] *GEANT 3.2.1*, CERN Computing Library (1993), http://wwwasdoc.web.cern.ch/wwwasdoc/pdfdir/geant.pdf.

[45] A. Drees and Z. Xu, Proceedings of the 2001 Particle Accelerator Conference, Chicago p. 3120 (2001).

[46] A. Adare et al. (PHENIX Collaboration), Phys. Rev. C **77**, 064907 (2008), 0801.1665.

[47] W. Vogelsang, private communication (2009).

[48] A. M. Rossi et al., Nucl. Phys. **B84**, 269 (1975).

[49] T. Alexopoulos et al. (E735 Collaboration), Phys. Rev. D **48**, 984 (1993).

[50] M. Kliemant, B. Lungwitz, and M. Gazdzicki, Phys. Rev. C **69**, 044903 (2004), hep-ex/0308002.

[51] J. Adams et al. (STAR Collaboration), Phys. Lett. **B616**, 8 (2005), nucl-ex/0309012.

[52] C. Tsallis, J. Stat. Phys. **52**, 479 (1988).

[53] T. Alexopoulos et al., Phys. Rev. Lett. **64**, 991 (1990).

[54] R. E. Ansorge et al. (UA5 Collaboration), Nucl. Phys. **B328**, 36 (1989).

[55] M. L. Miller, K. Reygers, S. J. Sanders, and P. Steinberg, Ann. Rev. Nucl. Part. Sci. **57**, 205 (2007), nucl-ex/0701025.

[56] B. Z. Kopeliovich, Phys. Rev. C **68**, 044906 (2003), nucl-th/0306044.

[57] B. Z. Kopeliovich, private communication (2010).

[58] K. Aamodt et al. (ALICE Collaboration) (2010), arXiv:1004.3034 [hep-ex].

[59] A. Adare et al. (PHENIX Collaboration), Phys. Rev. Lett. **101**, 232301 (2008), 0801.4020.

[60] S. S. Adler et al. (PHENIX Collaboration), Phys. Rev. Lett. **91**, 072301 (2003), nucl-ex/0304022.

[61] K. Adcox et al. (PHENIX Collaboration), Nucl. Phys. **A757**, 184 (2005), nucl-ex/0410003.

[62] S. S. Adler et al. (PHENIX Collaboration), Phys. Rev. Lett. **91**, 172301 (2003), nucl-ex/0305036.

[63] R. J. Fries, B. Muller, C. Nonaka, and S. A. Bass, Phys. Rev. Lett. **90**, 202303 (2003), nucl-th/0301087.

[64] R. C. Hwa and C. B. Yang, Phys. Rev. C **67**, 034902 (2003), nucl-th/0211010.

[65] V. Greco, C. M. Ko, and P. Levai, Phys. Rev. Lett. **90**, 202302 (2003), nucl-th/0301093.

[66] T. Hirano and Y. Nara, Phys. Rev. C **69**, 034908 (2004), nucl-th/0307015.

[67] K. Adcox et al. (PHENIX Collaboration), Phys. Rev. C **69**, 024904 (2004), nucl-ex/0307010.

[68] E. Schnedermann, J. Sollfrank, and U. W. Heinz, Phys. Rev. C **48**, 2462 (1993), nucl-th/9307020.

[69] T. Csörgő, S. V. Akkelin, Y. Hama, B. Lukács, and Y. M. Sinyukov, Phys. Rev. C **67**, 034904 (2003), hep-ph/0108067.

[70] F. Arleo, S. J. Brodsky, D. S. Hwang, and A. M. Sickles (2009), arXiv:0911.4604 [hep-ph].

[71] R. F. Cahalan, K. A. Geer, J. Kogut, and L. Susskind, Phys. Rev. D **11**, 1199 (1975).

[72] A. Clark et al., Phys. Lett. B **74**, 267 (1978).

[73] A. Angelis et al. (CCOR Collaboration), Phys. Lett. B **79**, 505 (1978).

[74] C. Kourkoumelis et al., Phys. Lett. B **84**, 271 (1979).

[75] M. Banner et al. (UA2 Collaboration), Phys. Lett. **115 B**, 1 (1982).

[76] J. Pumplin et al., J. High Energy Phys. **07**, 012 (2002).

[77] D. de Florian, R. Sassot, and M. Stratmann, Phys. Rev. D **75**, 114010 (2007).

[78] S. Albino, B. Kniehl, and G. Kramer, Nucl. Phys. **B725**, 181 (2005).

[79] B. Kniehl, G. Kramer, and B. Potter, Nucl. Phys. **B597**, 337 (2001).

Appendix A: Table of cross sections

The cross sections for $\pi^\pm$, $K^\pm$, p and $\overline{p}$ in $p+p$ collisions at $\sqrt{s} = 200$ and 62.4 GeV at midrapidity are tabulated in Tables XI – XVIII. Statistical and systematic uncertainties are also shown. The normalization uncertainty (9.7% for 200 GeV, 11% for 62.4 GeV) is not included. For protons and antiprotons, there are two kinds of tables, i.e. with and without the feed-down weak decay corrections.

TABLE XI: π^+ and π^- cross sections ($E\frac{d^3\sigma}{dp^3}$ [mb GeV$^{-2}c^3$]) in $p+p$ collisions at $\sqrt{s}=200$ GeV. Statistical (2nd column) and systematic (3rd column) uncertainties are shown for each particle species. The normalization uncertainty (9.7%) is not included.

p_T [GeV/c]	π^+	π^-
0.35	2.77e+01 ± 3.0e-01 ± 1.9e+00	2.63e+01 ± 3.7e-01 ± 1.8e+00
0.45	1.45e+01 ± 1.5e-01 ± 1.0e+00	1.40e+01 ± 2.0e-01 ± 9.8e-01
0.55	7.76e+00 ± 8.6e-02 ± 5.4e-01	7.91e+00 ± 1.2e-01 ± 5.5e-01
0.65	4.39e+00 ± 5.3e-02 ± 3.1e-01	4.44e+00 ± 7.0e-02 ± 3.1e-01
0.75	2.65e+00 ± 3.5e-02 ± 1.9e-01	2.69e+00 ± 4.6e-02 ± 1.9e-01
0.85	1.59e+00 ± 2.2e-02 ± 1.1e-01	1.60e+00 ± 2.9e-02 ± 1.1e-01
0.95	1.01e+00 ± 1.5e-02 ± 7.1e-02	9.83e-01 ± 1.9e-02 ± 6.9e-02
1.05	6.45e-01 ± 1.1e-02 ± 4.5e-02	6.30e-01 ± 1.3e-02 ± 4.4e-02
1.15	4.18e-01 ± 7.2e-03 ± 2.9e-02	4.36e-01 ± 9.5e-03 ± 3.1e-02
1.25	2.76e-01 ± 5.0e-03 ± 1.9e-02	2.79e-01 ± 6.3e-03 ± 2.0e-02
1.35	1.88e-01 ± 3.6e-03 ± 1.3e-02	1.90e-01 ± 4.4e-03 ± 1.3e-02
1.45	1.29e-01 ± 2.6e-03 ± 9.0e-03	1.29e-01 ± 3.1e-03 ± 9.0e-03
1.55	9.07e-02 ± 1.9e-03 ± 6.4e-03	9.05e-02 ± 2.3e-03 ± 6.3e-03
1.65	6.52e-02 ± 1.4e-03 ± 4.6e-03	6.47e-02 ± 1.7e-03 ± 4.5e-03
1.75	4.48e-02 ± 9.9e-04 ± 3.1e-03	4.69e-02 ± 1.2e-03 ± 3.3e-03
1.85	3.45e-02 ± 8.1e-04 ± 2.4e-03	3.40e-02 ± 9.3e-04 ± 2.4e-03
1.95	2.49e-02 ± 6.1e-04 ± 1.7e-03	2.56e-02 ± 7.4e-04 ± 1.8e-03
2.05	1.83e-02 ± 4.7e-04 ± 1.3e-03	1.81e-02 ± 5.5e-04 ± 1.3e-03
2.15	1.37e-02 ± 3.8e-04 ± 9.6e-04	1.33e-02 ± 4.3e-04 ± 9.3e-04
2.25	1.13e-02 ± 3.5e-04 ± 7.9e-04	1.03e-02 ± 3.6e-04 ± 7.2e-04
2.35	8.21e-03 ± 2.8e-04 ± 5.7e-04	7.48e-03 ± 2.8e-04 ± 5.2e-04
2.45	6.73e-03 ± 2.5e-04 ± 4.7e-04	6.34e-03 ± 2.7e-04 ± 4.4e-04
2.55	5.39e-03 ± 2.3e-04 ± 3.8e-04	4.96e-03 ± 2.3e-04 ± 3.5e-04
2.65	4.27e-03 ± 2.0e-04 ± 3.0e-04	3.47e-03 ± 1.8e-04 ± 2.4e-04
2.75	3.02e-03 ± 1.6e-04 ± 2.1e-04	2.82e-03 ± 1.6e-04 ± 2.0e-04
2.85	2.45e-03 ± 1.4e-04 ± 1.7e-04	2.23e-03 ± 1.5e-04 ± 1.6e-04
2.95	1.82e-03 ± 1.2e-04 ± 1.3e-04	1.66e-03 ± 1.2e-04 ± 1.2e-04

TABLE XII: K^+ and K^- cross sections ($E\frac{d^3\sigma}{dp^3}$ [mb GeV$^{-2}c^3$]) in $p+p$ collisions at $\sqrt{s}=200$ GeV. Statistical (2nd column) and systematic (3rd column) uncertainties are shown for each particle species. The normalization uncertainty (9.7%) is not included.

p_T [GeV/c]	K^+	K^-
0.45	1.96e+00 ± 5.0e-02 ± 1.4e-01	1.89e+00 ± 7.0e-02 ± 1.3e-01
0.55	1.35e+00 ± 3.0e-02 ± 9.4e-02	1.37e+00 ± 4.3e-02 ± 9.6e-02
0.65	8.71e-01 ± 1.9e-02 ± 6.1e-02	8.28e-01 ± 2.3e-02 ± 5.8e-02
0.75	5.86e-01 ± 1.3e-02 ± 4.1e-02	5.60e-01 ± 1.6e-02 ± 3.9e-02
0.85	3.95e-01 ± 8.7e-03 ± 2.8e-02	3.87e-01 ± 1.1e-02 ± 2.7e-02
0.95	2.60e-01 ± 5.8e-03 ± 1.8e-02	2.54e-01 ± 7.3e-03 ± 1.8e-02
1.05	1.72e-01 ± 3.9e-03 ± 1.2e-02	1.83e-01 ± 5.5e-03 ± 1.3e-02
1.15	1.26e-01 ± 3.0e-03 ± 8.9e-03	1.16e-01 ± 3.5e-03 ± 8.1e-03
1.25	8.52e-02 ± 2.1e-03 ± 6.0e-03	8.97e-02 ± 2.8e-03 ± 6.3e-03
1.35	6.08e-02 ± 1.5e-03 ± 4.3e-03	6.23e-02 ± 2.0e-03 ± 4.4e-03
1.45	4.59e-02 ± 1.2e-03 ± 3.2e-03	4.27e-02 ± 1.4e-03 ± 3.0e-03
1.55	3.29e-02 ± 9.0e-04 ± 2.3e-03	3.21e-02 ± 1.1e-03 ± 2.2e-03
1.65	2.39e-02 ± 6.6e-04 ± 1.7e-03	2.23e-02 ± 7.4e-04 ± 1.6e-03
1.75	1.86e-02 ± 5.3e-04 ± 1.3e-03	1.81e-02 ± 6.2e-04 ± 1.3e-03
1.85	1.49e-02 ± 4.4e-04 ± 1.0e-03	1.36e-02 ± 4.7e-04 ± 9.5e-04
1.95	1.13e-02 ± 3.5e-04 ± 7.9e-04	1.03e-02 ± 3.7e-04 ± 7.2e-04

TABLE XIII: p and $\overline{p}$ cross sections ($E\frac{d^3\sigma}{dp^3}$ [mb GeV$^{-2}c^3$]) in $p + p$ collisions at $\sqrt{s} = 200$ GeV. Statistical (2nd column) and systematic (3rd column) uncertainties are shown for each particle species. The normalization uncertainty (9.7%) is not included. Feed-down weak decay corrections are not applied.

p_T [GeV/c]	p	$\overline{p}$
0.55	1.02e+00 $\pm$ 2.0e-02 $\pm$ 6.2e-02	7.88e-01 $\pm$ 1.6e-02 $\pm$ 5.5e-02
0.65	7.40e-01 $\pm$ 1.4e-02 $\pm$ 4.5e-02	6.04e-01 $\pm$ 1.2e-02 $\pm$ 4.2e-02
0.75	5.58e-01 $\pm$ 1.1e-02 $\pm$ 3.4e-02	4.62e-01 $\pm$ 9.1e-03 $\pm$ 3.2e-02
0.85	3.77e-01 $\pm$ 7.7e-03 $\pm$ 2.3e-02	3.18e-01 $\pm$ 6.3e-03 $\pm$ 2.2e-02
0.95	2.73e-01 $\pm$ 5.9e-03 $\pm$ 1.6e-02	2.18e-01 $\pm$ 4.4e-03 $\pm$ 1.5e-02
1.05	1.80e-01 $\pm$ 4.0e-03 $\pm$ 1.1e-02	1.58e-01 $\pm$ 3.3e-03 $\pm$ 1.1e-02
1.15	1.27e-01 $\pm$ 2.9e-03 $\pm$ 7.6e-03	1.08e-01 $\pm$ 2.4e-03 $\pm$ 7.6e-03
1.25	9.18e-02 $\pm$ 2.2e-03 $\pm$ 5.5e-03	7.54e-02 $\pm$ 1.7e-03 $\pm$ 5.3e-03
1.35	6.24e-02 $\pm$ 1.6e-03 $\pm$ 3.7e-03	5.58e-02 $\pm$ 1.3e-03 $\pm$ 3.9e-03
1.45	4.80e-02 $\pm$ 1.3e-03 $\pm$ 2.9e-03	3.73e-02 $\pm$ 8.9e-04 $\pm$ 2.6e-03
1.55	3.32e-02 $\pm$ 9.1e-04 $\pm$ 2.0e-03	2.68e-02 $\pm$ 6.6e-04 $\pm$ 1.9e-03
1.65	2.31e-02 $\pm$ 6.5e-04 $\pm$ 1.4e-03	1.93e-02 $\pm$ 4.9e-04 $\pm$ 1.4e-03
1.75	1.70e-02 $\pm$ 5.0e-04 $\pm$ 1.0e-03	1.39e-02 $\pm$ 3.7e-04 $\pm$ 9.8e-04
1.85	1.17e-02 $\pm$ 3.6e-04 $\pm$ 7.0e-04	9.69e-03 $\pm$ 2.6e-04 $\pm$ 6.8e-04
1.95	8.98e-03 $\pm$ 2.9e-04 $\pm$ 5.4e-04	6.94e-03 $\pm$ 1.9e-04 $\pm$ 4.9e-04
2.05	6.68e-03 $\pm$ 2.3e-04 $\pm$ 4.0e-04	5.12e-03 $\pm$ 1.5e-04 $\pm$ 3.6e-04
2.15	4.62e-03 $\pm$ 1.6e-04 $\pm$ 2.8e-04	3.61e-03 $\pm$ 1.1e-04 $\pm$ 2.5e-04
2.25	3.91e-03 $\pm$ 1.5e-04 $\pm$ 2.4e-04	2.90e-03 $\pm$ 9.2e-05 $\pm$ 2.0e-04
2.35	2.63e-03 $\pm$ 1.0e-04 $\pm$ 1.6e-04	2.09e-03 $\pm$ 7.0e-05 $\pm$ 1.5e-04
2.45	1.79e-03 $\pm$ 7.4e-05 $\pm$ 1.1e-04	1.58e-03 $\pm$ 5.5e-05 $\pm$ 1.1e-04
2.55	1.62e-03 $\pm$ 7.0e-05 $\pm$ 1.0e-04	1.10e-03 $\pm$ 4.2e-05 $\pm$ 7.8e-05
2.65	1.15e-03 $\pm$ 5.4e-05 $\pm$ 7.2e-05	8.85e-04 $\pm$ 3.7e-05 $\pm$ 6.3e-05
2.75	8.89e-04 $\pm$ 4.4e-05 $\pm$ 5.6e-05	6.22e-04 $\pm$ 2.8e-05 $\pm$ 4.4e-05
2.85	6.38e-04 $\pm$ 3.5e-05 $\pm$ 4.1e-05	5.07e-04 $\pm$ 2.4e-05 $\pm$ 3.6e-05
2.95	4.97e-04 $\pm$ 3.0e-05 $\pm$ 3.2e-05	3.80e-04 $\pm$ 2.0e-05 $\pm$ 2.7e-05
3.05	4.13e-04 $\pm$ 2.6e-05 $\pm$ 2.7e-05	3.13e-04 $\pm$ 1.7e-05 $\pm$ 2.3e-05
3.10	3.80e-04 $\pm$ 1.8e-05 $\pm$ 2.5e-05	2.75e-04 $\pm$ 1.1e-05 $\pm$ 2.0e-05
3.30	2.33e-04 $\pm$ 1.3e-05 $\pm$ 1.6e-05	1.92e-04 $\pm$ 9.0e-06 $\pm$ 1.4e-05
3.50	1.57e-04 $\pm$ 1.0e-05 $\pm$ 1.1e-05	1.12e-04 $\pm$ 6.5e-06 $\pm$ 8.6e-06
3.70	1.11e-04 $\pm$ 8.9e-06 $\pm$ 8.3e-06	7.16e-05 $\pm$ 5.2e-06 $\pm$ 5.8e-06
3.90	7.25e-05 $\pm$ 7.2e-06 $\pm$ 5.8e-06	4.40e-05 $\pm$ 4.0e-06 $\pm$ 3.8e-06
4.10	6.23e-05 $\pm$ 6.7e-06 $\pm$ 5.3e-06	3.81e-05 $\pm$ 3.9e-06 $\pm$ 3.6e-06
4.30	3.83e-05 $\pm$ 5.5e-06 $\pm$ 3.6e-06	2.63e-05 $\pm$ 3.3e-06 $\pm$ 2.8e-06
4.50	3.22e-05 $\pm$ 5.2e-06 $\pm$ 3.3e-06	1.82e-05 $\pm$ 2.8e-06 $\pm$ 2.2e-06

TABLE XIV: p and $\overline{p}$ cross sections ($E\frac{d^3\sigma}{dp^3}$ [mb GeV$^{-2}c^3$]) in $p + p$ collisions at $\sqrt{s} = 200$ GeV. Statistical (2nd column) and systematic (3rd column) uncertainties are shown for each particle species. The normalization uncertainty (9.7%) is not included. Feed-down weak decay corrections are applied.

p_T [GeV/c]	p	$\overline{p}$
0.55	5.93e-01 ± 1.1e-02 ± 1.4e-01	4.56e-01 ± 9.2e-03 ± 1.1e-01
0.65	4.45e-01 ± 8.4e-03 ± 9.4e-02	3.63e-01 ± 7.0e-03 ± 7.8e-02
0.75	3.47e-01 ± 6.9e-03 ± 6.6e-02	2.87e-01 ± 5.6e-03 ± 5.6e-02
0.85	2.42e-01 ± 4.9e-03 ± 4.2e-02	2.04e-01 ± 4.0e-03 ± 3.6e-02
0.95	1.80e-01 ± 3.9e-03 ± 2.9e-02	1.44e-01 ± 2.9e-03 ± 2.4e-02
1.05	1.22e-01 ± 2.7e-03 ± 1.8e-02	1.06e-01 ± 2.2e-03 ± 1.6e-02
1.15	8.77e-02 ± 2.0e-03 ± 1.2e-02	7.48e-02 ± 1.6e-03 ± 1.1e-02
1.25	6.46e-02 ± 1.6e-03 ± 8.4e-03	5.31e-02 ± 1.2e-03 ± 7.1e-03
1.35	4.47e-02 ± 1.1e-03 ± 5.5e-03	4.00e-02 ± 9.4e-04 ± 5.1e-03
1.45	3.49e-02 ± 9.4e-04 ± 4.1e-03	2.72e-02 ± 6.5e-04 ± 3.3e-03
1.55	2.45e-02 ± 6.8e-04 ± 2.7e-03	1.98e-02 ± 4.9e-04 ± 2.3e-03
1.65	1.73e-02 ± 4.9e-04 ± 1.9e-03	1.45e-02 ± 3.7e-04 ± 1.6e-03
1.75	1.28e-02 ± 3.8e-04 ± 1.3e-03	1.06e-02 ± 2.8e-04 ± 1.2e-03
1.85	8.92e-03 ± 2.7e-04 ± 8.9e-04	7.42e-03 ± 2.0e-04 ± 7.9e-04
1.95	6.95e-03 ± 2.2e-04 ± 6.8e-04	5.37e-03 ± 1.5e-04 ± 5.6e-04
2.05	5.21e-03 ± 1.8e-04 ± 4.9e-04	4.00e-03 ± 1.2e-04 ± 4.0e-04
2.15	3.63e-03 ± 1.3e-04 ± 3.4e-04	2.84e-03 ± 8.7e-05 ± 2.8e-04
2.25	3.10e-03 ± 1.2e-04 ± 2.8e-04	2.30e-03 ± 7.3e-05 ± 2.2e-04
2.35	2.10e-03 ± 8.2e-05 ± 1.9e-04	1.67e-03 ± 5.6e-05 ± 1.6e-04
2.45	1.44e-03 ± 6.0e-05 ± 1.3e-04	1.27e-03 ± 4.4e-05 ± 1.2e-04
2.55	1.31e-03 ± 5.7e-05 ± 1.1e-04	8.89e-04 ± 3.4e-05 ± 8.3e-05
2.65	9.31e-04 ± 4.4e-05 ± 8.0e-05	7.19e-04 ± 3.0e-05 ± 6.6e-05
2.75	7.26e-04 ± 3.6e-05 ± 6.2e-05	5.08e-04 ± 2.3e-05 ± 4.6e-05
2.85	5.23e-04 ± 2.9e-05 ± 4.4e-05	4.16e-04 ± 2.0e-05 ± 3.8e-05
2.95	4.09e-04 ± 2.4e-05 ± 3.4e-05	3.13e-04 ± 1.6e-05 ± 2.8e-05
3.05	3.41e-04 ± 2.2e-05 ± 2.9e-05	2.58e-04 ± 1.4e-05 ± 2.3e-05
3.10	3.14e-04 ± 1.5e-05 ± 2.6e-05	2.28e-04 ± 9.3e-06 ± 2.0e-05
3.30	1.94e-04 ± 1.1e-05 ± 1.6e-05	1.60e-04 ± 7.5e-06 ± 1.4e-05
3.50	1.32e-04 ± 8.6e-06 ± 1.1e-05	9.42e-05 ± 5.4e-06 ± 8.6e-06
3.70	9.35e-05 ± 7.5e-06 ± 8.2e-06	6.03e-05 ± 4.4e-06 ± 5.6e-06
3.90	6.13e-05 ± 6.1e-06 ± 5.6e-06	3.72e-05 ± 3.4e-06 ± 3.6e-06
4.10	5.28e-05 ± 5.7e-06 ± 5.1e-06	3.24e-05 ± 3.3e-06 ± 3.4e-06
4.30	3.26e-05 ± 4.7e-06 ± 3.3e-06	2.23e-05 ± 2.8e-06 ± 2.6e-06
4.50	2.75e-05 ± 4.4e-06 ± 3.0e-06	1.56e-05 ± 2.4e-06 ± 2.0e-06

TABLE XV: π^+ and π^- cross sections ($E\frac{d^3\sigma}{dp^3}$ [mb GeV$^{-2}c^3$]) in $p + p$ collisions at $\sqrt{s} = 62.4$ GeV. Statistical (2nd column) and systematic (3rd column) uncertainties are shown for each particle species. The normalization uncertainty (11%) is not included.

p_T [GeV/c]	π^+	π^-
0.35	1.96e+01 $\pm$ 1.8e-01 $\pm$ 1.4e+00	2.08e+01 $\pm$ 1.5e-01 $\pm$ 1.3e+00
0.45	1.07e+01 $\pm$ 1.1e-01 $\pm$ 7.5e-01	1.12e+01 $\pm$ 8.6e-02 $\pm$ 6.7e-01
0.55	5.95e+00 $\pm$ 6.3e-02 $\pm$ 4.2e-01	5.94e+00 $\pm$ 4.9e-02 $\pm$ 3.6e-01
0.65	3.38e+00 $\pm$ 3.9e-02 $\pm$ 2.4e-01	3.25e+00 $\pm$ 3.0e-02 $\pm$ 1.9e-01
0.75	1.91e+00 $\pm$ 2.4e-02 $\pm$ 1.3e-01	1.92e+00 $\pm$ 2.0e-02 $\pm$ 1.2e-01
0.85	1.13e+00 $\pm$ 1.6e-02 $\pm$ 7.9e-02	1.15e+00 $\pm$ 1.3e-02 $\pm$ 6.9e-02
0.95	6.86e-01 $\pm$ 1.0e-02 $\pm$ 4.8e-02	6.68e-01 $\pm$ 8.4e-03 $\pm$ 4.0e-02
1.05	4.30e-01 $\pm$ 7.2e-03 $\pm$ 3.0e-02	4.06e-01 $\pm$ 5.7e-03 $\pm$ 2.4e-02
1.15	2.65e-01 $\pm$ 4.9e-03 $\pm$ 1.9e-02	2.53e-01 $\pm$ 4.0e-03 $\pm$ 1.5e-02
1.25	1.66e-01 $\pm$ 3.5e-03 $\pm$ 1.2e-02	1.60e-01 $\pm$ 2.9e-03 $\pm$ 9.6e-03
1.35	1.08e-01 $\pm$ 2.6e-03 $\pm$ 7.5e-03	1.03e-01 $\pm$ 2.1e-03 $\pm$ 6.2e-03
1.45	7.20e-02 $\pm$ 1.9e-03 $\pm$ 5.0e-03	6.74e-02 $\pm$ 1.6e-03 $\pm$ 4.0e-03
1.55	5.04e-02 $\pm$ 1.5e-03 $\pm$ 3.5e-03	4.54e-02 $\pm$ 1.2e-03 $\pm$ 2.7e-03
1.65	3.48e-02 $\pm$ 1.2e-03 $\pm$ 2.4e-03	3.07e-02 $\pm$ 9.7e-04 $\pm$ 1.8e-03
1.75	2.33e-02 $\pm$ 9.5e-04 $\pm$ 1.6e-03	2.25e-02 $\pm$ 8.3e-04 $\pm$ 1.4e-03
1.85	1.58e-02 $\pm$ 7.8e-04 $\pm$ 1.1e-03	1.55e-02 $\pm$ 6.8e-04 $\pm$ 9.3e-04
1.95	1.11e-02 $\pm$ 6.7e-04 $\pm$ 7.8e-04	9.63e-03 $\pm$ 5.2e-04 $\pm$ 5.8e-04
2.05	7.13e-03 $\pm$ 5.2e-04 $\pm$ 5.0e-04	7.23e-03 $\pm$ 4.7e-04 $\pm$ 4.3e-04
2.15	5.63e-03 $\pm$ 5.0e-04 $\pm$ 4.0e-04	4.72e-03 $\pm$ 3.9e-04 $\pm$ 2.9e-04
2.25	4.22e-03 $\pm$ 4.3e-04 $\pm$ 3.0e-04	3.32e-03 $\pm$ 3.4e-04 $\pm$ 2.0e-04
2.35	2.69e-03 $\pm$ 3.7e-04 $\pm$ 1.9e-04	2.67e-03 $\pm$ 3.3e-04 $\pm$ 1.7e-04
2.45	1.96e-03 $\pm$ 3.1e-04 $\pm$ 1.4e-04	1.75e-03 $\pm$ 2.9e-04 $\pm$ 1.1e-04
2.55	1.45e-03 $\pm$ 3.3e-04 $\pm$ 1.1e-04	1.49e-03 $\pm$ 2.7e-04 $\pm$ 9.8e-05
2.65	9.07e-04 $\pm$ 2.2e-04 $\pm$ 7.0e-05	1.07e-03 $\pm$ 2.5e-04 $\pm$ 7.3e-05
2.75	1.09e-03 $\pm$ 3.0e-04 $\pm$ 8.6e-05	7.62e-04 $\pm$ 2.5e-04 $\pm$ 5.4e-05
2.85	6.48e-04 $\pm$ 2.3e-04 $\pm$ 5.3e-05	5.10e-04 $\pm$ 2.0e-04 $\pm$ 3.7e-05

TABLE XVI: K^+ and K^- cross sections ($E\frac{d^3\sigma}{dp^3}$ [mb GeV$^{-2}c^3$]) in $p+p$ collisions at $\sqrt{s} = 62.4$ GeV. Statistical (2nd column) and systematic (3rd column) uncertainties are shown for each particle species. The normalization uncertainty (11%) is not included.

p_T [GeV/c]	K^+	K^-
0.45	1.18e+00 ± 2.7e-02 ± 8.2e-02	1.06e+00 ± 1.9e-02 ± 7.4e-02
0.55	8.18e-01 ± 1.8e-02 ± 5.7e-02	7.48e-01 ± 1.3e-02 ± 5.2e-02
0.65	6.07e-01 ± 1.3e-02 ± 4.3e-02	5.30e-01 ± 9.6e-03 ± 3.7e-02
0.75	3.72e-01 ± 8.4e-03 ± 2.6e-02	3.43e-01 ± 6.7e-03 ± 2.4e-02
0.85	2.50e-01 ± 6.1e-03 ± 1.8e-02	2.14e-01 ± 4.6e-03 ± 1.5e-02
0.95	1.73e-01 ± 4.7e-03 ± 1.2e-02	1.40e-01 ± 3.4e-03 ± 9.8e-03
1.05	1.12e-01 ± 3.3e-03 ± 7.8e-03	9.05e-02 ± 2.5e-03 ± 6.3e-03
1.15	7.94e-02 ± 2.7e-03 ± 5.6e-03	6.17e-02 ± 1.9e-03 ± 4.3e-03
1.25	4.88e-02 ± 1.9e-03 ± 3.4e-03	4.35e-02 ± 1.5e-03 ± 3.0e-03
1.35	3.41e-02 ± 1.5e-03 ± 2.4e-03	2.84e-02 ± 1.2e-03 ± 2.0e-03
1.45	2.45e-02 ± 1.2e-03 ± 1.7e-03	1.96e-02 ± 9.2e-04 ± 1.4e-03
1.55	1.63e-02 ± 9.5e-04 ± 1.1e-03	1.34e-02 ± 7.6e-04 ± 9.4e-04
1.65	1.28e-02 ± 8.0e-04 ± 9.1e-04	9.77e-03 ± 6.2e-04 ± 7.0e-04
1.75	9.56e-03 ± 6.8e-04 ± 7.1e-04	6.65e-03 ± 4.8e-04 ± 4.9e-04
1.85	6.34e-03 ± 5.4e-04 ± 5.0e-04	4.87e-03 ± 4.2e-04 ± 3.8e-04
1.95	5.28e-03 ± 5.1e-04 ± 4.4e-04	3.45e-03 ± 3.7e-04 ± 2.9e-04

TABLE XVII: p and $\overline{p}$ cross sections ($E\frac{d^3\sigma}{dp^3}$ [mb GeV$^{-2}c^3$]) in $p+p$ collisions at $\sqrt{s} = 62.4$ GeV. Statistical (2nd column) and systematic (3rd column) uncertainties are shown for each particle species. The normalization uncertainty (11%) is not included. Feed-down weak decay corrections are not applied.

p_T [GeV/c]	p	$\overline{p}$
0.65	4.63e-01 ± 7.1e-03 ± 4.2e-02	3.09e-01 ± 4.6e-03 ± 2.2e-02
0.75	3.28e-01 ± 5.4e-03 ± 3.0e-02	2.19e-01 ± 3.6e-03 ± 1.5e-02
0.85	2.49e-01 ± 4.5e-03 ± 2.2e-02	1.59e-01 ± 2.9e-03 ± 1.1e-02
0.95	1.69e-01 ± 3.4e-03 ± 1.5e-02	1.10e-01 ± 2.3e-03 ± 7.7e-03
1.05	1.20e-01 ± 2.7e-03 ± 1.1e-02	7.50e-02 ± 1.8e-03 ± 5.3e-03
1.15	8.12e-02 ± 2.1e-03 ± 7.3e-03	4.95e-02 ± 1.4e-03 ± 3.5e-03
1.25	5.81e-02 ± 1.7e-03 ± 5.2e-03	3.32e-02 ± 1.1e-03 ± 2.3e-03
1.35	3.95e-02 ± 1.4e-03 ± 3.6e-03	2.37e-02 ± 9.4e-04 ± 1.7e-03
1.45	2.55e-02 ± 9.9e-04 ± 2.3e-03	1.53e-02 ± 7.1e-04 ± 1.1e-03
1.55	1.84e-02 ± 8.4e-04 ± 1.7e-03	1.07e-02 ± 6.0e-04 ± 7.5e-04
1.65	1.37e-02 ± 7.2e-04 ± 1.2e-03	7.03e-03 ± 4.7e-04 ± 4.9e-04
1.75	9.31e-03 ± 5.8e-04 ± 8.4e-04	4.49e-03 ± 3.7e-04 ± 3.1e-04
1.85	5.90e-03 ± 4.4e-04 ± 5.3e-04	3.39e-03 ± 3.4e-04 ± 2.4e-04
1.95	4.02e-03 ± 3.6e-04 ± 3.6e-04	2.12e-03 ± 2.4e-04 ± 1.5e-04
2.05	3.11e-03 ± 3.1e-04 ± 2.8e-04	1.58e-03 ± 2.2e-04 ± 1.1e-04
2.15	1.99e-03 ± 2.5e-04 ± 1.8e-04	1.04e-03 ± 1.7e-04 ± 7.3e-05
2.25	1.37e-03 ± 2.1e-04 ± 1.2e-04	6.99e-04 ± 1.5e-04 ± 4.9e-05
2.35	8.94e-04 ± 1.5e-04 ± 8.0e-05	5.90e-04 ± 1.3e-04 ± 4.1e-05
2.45	6.34e-04 ± 1.3e-04 ± 5.7e-05	3.13e-04 ± 1.1e-04 ± 2.2e-05
2.55	6.33e-04 ± 1.4e-04 ± 5.7e-05	2.43e-04 ± 8.3e-05 ± 1.7e-05
2.65	4.56e-04 ± 1.2e-04 ± 4.1e-05	1.80e-04 ± 7.9e-05 ± 1.3e-05
2.75	4.11e-04 ± 1.1e-04 ± 3.7e-05	1.74e-04 ± 7.5e-05 ± 1.2e-05
2.85	2.40e-04 ± 9.5e-05 ± 2.2e-05	2.39e-04 ± 9.1e-05 ± 1.7e-05
2.95	1.63e-04 ± 6.6e-05 ± 1.5e-05	6.57e-05 ± 5.0e-05 ± 4.7e-06
3.10	9.65e-05 ± 3.7e-05 ± 8.9e-06	7.07e-05 ± 2.8e-05 ± 5.1e-06
3.30	9.05e-05 ± 4.1e-05 ± 8.5e-06	4.14e-05 ± 3.2e-05 ± 3.1e-06
3.50	2.13e-05 ± 1.9e-05 ± 2.0e-06	5.21e-05 ± 3.2e-05 ± 4.0e-06

TABLE XVIII: p and $\overline{p}$ cross sections ($E\frac{d^3\sigma}{dp^3}$ [mb GeV$^{-2}c^3$]) in $p+p$ collisions at $\sqrt{s} = 62.4$ GeV. Statistical (2nd column) and systematic (3rd column) uncertainties are shown for each particle species. The normalization uncertainty (11%) is not included. Feed-down weak decay corrections are applied.

p_T [GeV/c]	p	$\overline{p}$
0.65	2.95e-01 ± 4.5e-03 ± 6.6e-02	1.18e-01 ± 1.8e-03 ± 6.5e-02
0.75	2.38e-01 ± 3.9e-03 ± 3.8e-02	1.20e-01 ± 2.0e-03 ± 3.4e-02
0.85	1.96e-01 ± 3.5e-03 ± 2.5e-02	1.05e-01 ± 1.9e-03 ± 1.9e-02
0.95	1.40e-01 ± 2.8e-03 ± 1.6e-02	8.12e-02 ± 1.7e-03 ± 1.1e-02
1.05	1.03e-01 ± 2.3e-03 ± 1.1e-02	5.91e-02 ± 1.4e-03 ± 6.6e-03
1.15	7.18e-02 ± 1.9e-03 ± 7.1e-03	4.07e-02 ± 1.1e-03 ± 4.0e-03
1.25	5.23e-02 ± 1.5e-03 ± 5.1e-03	2.81e-02 ± 9.4e-04 ± 2.6e-03
1.35	3.60e-02 ± 1.2e-03 ± 3.4e-03	2.04e-02 ± 8.1e-04 ± 1.8e-03
1.45	2.34e-02 ± 9.1e-04 ± 2.2e-03	1.33e-02 ± 6.2e-04 ± 1.1e-03
1.55	1.70e-02 ± 7.7e-04 ± 1.6e-03	9.42e-03 ± 5.2e-04 ± 7.8e-04
1.65	1.27e-02 ± 6.7e-04 ± 1.2e-03	6.19e-03 ± 4.1e-04 ± 5.1e-04
1.75	8.67e-03 ± 5.4e-04 ± 8.1e-04	3.97e-03 ± 3.3e-04 ± 3.2e-04
1.85	5.51e-03 ± 4.1e-04 ± 5.1e-04	3.00e-03 ± 3.0e-04 ± 2.4e-04
1.95	3.76e-03 ± 3.3e-04 ± 3.5e-04	1.88e-03 ± 2.2e-04 ± 1.5e-04
2.05	2.91e-03 ± 2.9e-04 ± 2.7e-04	1.41e-03 ± 2.0e-04 ± 1.1e-04
2.15	1.86e-03 ± 2.4e-04 ± 1.7e-04	9.24e-04 ± 1.5e-04 ± 7.4e-05
2.25	1.28e-03 ± 2.0e-04 ± 1.2e-04	6.21e-04 ± 1.3e-04 ± 5.0e-05
2.35	8.39e-04 ± 1.4e-04 ± 7.7e-05	5.25e-04 ± 1.2e-04 ± 4.2e-05
2.45	5.95e-04 ± 1.2e-04 ± 5.5e-05	2.78e-04 ± 9.4e-05 ± 2.2e-05
2.55	5.94e-04 ± 1.3e-04 ± 5.5e-05	2.16e-04 ± 7.4e-05 ± 1.7e-05
2.65	4.28e-04 ± 1.1e-04 ± 3.9e-05	1.60e-04 ± 7.0e-05 ± 1.3e-05
2.75	3.86e-04 ± 1.1e-04 ± 3.6e-05	1.55e-04 ± 6.6e-05 ± 1.2e-05
2.85	2.25e-04 ± 8.9e-05 ± 2.1e-05	2.13e-04 ± 8.1e-05 ± 1.7e-05
2.95	1.54e-04 ± 6.2e-05 ± 1.4e-05	5.85e-05 ± 4.4e-05 ± 4.7e-06
3.10	9.06e-05 ± 3.4e-05 ± 8.5e-06	6.30e-05 ± 2.5e-05 ± 5.2e-06
3.30	8.50e-05 ± 3.8e-05 ± 8.1e-06	3.69e-05 ± 2.8e-05 ± 3.1e-06
3.50	2.00e-05 ± 1.7e-05 ± 2.0e-06	4.64e-05 ± 2.8e-05 ± 4.0e-06